Development of Chloromethyl Functionalized Poly(3,4-ethylenedioxythiophene) Derivative (PEDOT-MeCl:PSS) Hole Transport Layer for Perovskite Solar Cells

Zhiyin Niu

A thesis

Submitted in partial fulfillment of the

Requirements for the degree of

Mater of Science in Chemical Engineering

University of Washington

2019

Reading Committee:

Qiuming Yu, Chair

Rene Overney

Program Authorized to Offer Degree:

Chemical Engineering

University of Washington

Abstract

Development of Chloromethyl Functionalized Poly(3,4-ethylenedioxythiophene) Derivative (PEDOT-MeCl:PSS) Hole Transport Layer for Perovskite Solar Cells

Zhiyin Niu

Chair of the Supervisory Committee:

Professor Qiuming Yu

Department of Chemical Engineering

Highly efficient planar perovskite solar cells with a chloromethyl functionalized poly(3,4-ethylenedioxythiophene) derivative (PEDOT-MeCl:PSS) as hole transport layer (HTL) were developed. A combination of characterization techniques was employed to investigate the effects of chloromethyl function group on the electron donation capability of PEDOT-MeCl:PSS, perovskite film quality and charge recombination kinetics in the solar cells. Our study shows that the presence of chloromethyl group at the PEDOT-MeCl surface gives the HTL a desirable energy level alignment with perovskite. The favorable interaction between the chlorine and perovskite provides a better crystal with less PbI_2 comparing with PEDOT:PSS. As a result, better device performance with higher short-circuit current density (Jsc) and fill factor (FF) was gained, leading to better power conversion efficiency. Our study provides an insight to the development of new hole transport materials for high efficiency perovskite solar cells.

TABLE OF CONTENTS

LIST OF FIGURES

ACKNOWLEDGEMENTS

First and foremost, I would like to show my deepest gratitude to my supervisor, Professor Qiuming Yu, a respectable, responsible and resourceful scholar, who has provided me with valuable guidance in every stage of the writing of this thesis. Her keen and vigorous academic observation enlightens me not only in this thesis but also in my future study. I also express my warmest gratitude to Professor Rene Overney who served on my Committee for my Master Thesis Defense. I am grateful for his time and insightful feedback.

I am grateful to my current and past lab mates in the Yu Group including Dr. Daniel David Galvan, Monica Esopi, Gabriella Tosado, Erjin Zheng, Yi-Yu Lin, Emerson Chen, Hao Dong, Zonglun Li, Zizhao Xu, Chen Cai, Wenxin Cao and ShukunZhong. Their comradery, support, and intellectual stimulus have been wonderful to be apart of, and I will truly miss sharing the lab with them.

Finally, I would like to thank all my friends and my family for their undiminishing support. I would like to say thank you to my parents and brother for their constant encouragement, and for instilling scientific curiosity in me at a young age. Finally, I would like to thank all my old friends back home in China, and all the new ones I made in Seattle for sharing great times together.

Chapter 1. INTRODUCTION

1.1 HYBRID PEROVSKITE SOLAR CELLS

Hybrid perovskite solar cells (PVSCs) show great potential as a renewable energy source due to the exceptional optoelectronic properties of perovskites, such as strong light adsorption[1] and high charge carrier mobility and length[2], and the possibility of low-cost, large-area solution processing of PVSCs[3, 4] to reduce manufacturing cost and energy input[5]. Certified state-of-the-art single-junction PVSCs have achieved power conversion efficiency (PCE) up to 23.3%[6]. Though exciting, more efforts are still needed to tackle the challenges faced in the transfer of PVSCs as a promising technology for clean energy. For instance, in addition to the perovskite materials and device architecture, the physical and electronic contacts between perovskite and electrode are known to affect the performance of PVSCs[7]. However, the structure-properties relationships of interfacial materials are less explored and their effects on device performance are also not well-established. PVSCs with a mesoporous structure based on a TiO_2 scaffold have been found to be highly efficient, but the high temperature (> 500℃) sintering required to construct a mesoporous TiO_2 scaffold inevitably hinders the development of low-cost devices[8-10]. With perovskite charge carrier diffusion lengths in micrometers, a simple planar structure based on either a regular (n-i-p) or inverted (p-i-n) layout has been developed and exhibit high performance[10-12]. The inverted architecture, wherein a perovskite semiconductor is sandwiched by poly(3,4-ethylenedioxythiophene): poly(styrenesulfonate) (PEDOT:PSS) as a hole transport layer (HTL) and phenyl-C61-butyric acid methyl ester (PCBM) as an electron transport layer (ETL), is particularly attractive due to its low-temperature solution processing and negligible hysteresis[13-18].

1.2 PEDOT:PSS AND ITS APPLICATION

PEDOT:PSS is a polymer electrolyte consisting of positively charged conjugated conducting PEDOT and negatively charged insulating PSS. The negatively charged, hydrophilic PSS functions as a dopant to the oxidized, positively charged PEDOT and also helps to disperse and stabilize the hydrophobic PEDOT in water. As one of the most successful conducting polymer in terms of practical applications, the commercially available PEDOT:PSS aqueous dispersion is a deep-blue opaque solution. It readily forms a continuous thin film on ether rigid or flexible substrates by various solution-processing techniques with a smooth surface with a transmittance above 90% in the visible light range[19]. The nice conductivity, high work function and good physical and chemical stability make PEDOT:PSS widely used in energy conservation and storage devices, namely organic solar cells[20], dye-sensitized solar cells[21], supercapacitors[22], fuel cells[23], as well as thermoelectric devices[24] and stretchable devices[25, 26].

1.3 PEDOT:PSS DERIVATIVS

Although PEDOT:PSS has many advantages as a HTL, it also has some disadvantages that cannot be ignored. For example, the lack of functional group is a large restriction in terms of applications. In the meanwhile, it is well known that the defects exist at the interface of PEDOT:PSS and perovskite will strongly hinder the device performance. Therefore, we hypothesized that by introducing a chloromethyl function group to the PEDOT backbone, the strong interaction between lead and chlorine[27, 28] could lead to forming a direct chemical bond between Cl and Pb and initiating the growth of perovskite, and thus reduce the interface defects and improve the device performance. In this work, we synthesized chloromethyl EDOT (EDOT-MeCl) monomers and polymerized them in the presence of PSS to obtain PEDOT-MeCl:PSS by oxidative chemical polymerization. We systematically studied the effects of the molar ratios of

oxidant and sodium hydroxide to the monomer, the concentration of monomers, and the reaction temperature and time on the polymerization reaction. Surface characterization techniques, such as contacting angle measurement, Raman Spectroscopy, and X-ray photoelectron spectroscopy (XPS), were used to characterized the content of PEDOT-MeCl both qualitatively and quantitatively. Besides, we also use the various characterization techniques to detect the film quality of perovskite. For instance, using scanning electron microscope (SEM) to characterize the surface morphology and grain size, X-ray diffraction (XRD) techniques were used to detect the surface crystal structures, the Ultraviolet-visible spectrophotometry (UV-vis) was used to detect the absorb spectrum, the time correlated single photon counting (TSCPC) technique was used to detect the perovskite decay lifetime on different hole transporting layers. Eventually, the device performance and physical properties were studied systematically for perovskite with planar p-i-n layout. The Jsc, FF, and PCE of the surface modified perovskite solar cells were found to increase simultaneously from 9.64 mA/cm^2, 71% and 7.46% to 12.92 mA/cm^2, 74% and 10.35%, respectively. These in-depth insights into structure and performance provide novel guidance for the design of HTLs, inspired by the electron transfer of semi-quinone radicals in phenol derivatives, to further improve the performance of inverted planar heterojunction PVSCs.

Chapter 2. EXPERIMENTAL METHODS

2.1 CHEMICALS

3，4-Ethylenedioxythiophene (EDOT, 97%), sodium persulfate ($Na_2S_2O_8$, ≥98%), iron(III) sulfate hydrate ($Fe_2(SO_4)_3 \cdot x\ H_2O$, 97%), poly (4-styrenesulfonic acid) solution (PSSH, Mw~75,000, 18 wt.% in H_2O), hydrochloric acid (HCl, 37%), 3,4-dimethoxythiophene (97%), 3-chloro-1,2-propanediol (98%), p-toluenesulfonic acid monohydrate (PTSA, ≥ 98.5%), lead(II) iodide (PbI_2, 99.9%), toluene (anhydrous, 99.8%), chloroform (≥ 99.99%), γ-butyrolactone (GBL, ≥ 99%), *N,N*-dimethyl sulfoxide (DMSO, anhydrous, ≥ 99.9%), and bathocuproine (BCP, 96%) were purchased from Sigma-Aldrich. Sodium hydroxide (NaOH) and dichloromethane(DCM) were purchased from Fisher Scientific. PEDOT:PSS (Clevios P VP Al 4083) was obtained from H.C. Starck. Methylammonium iodide (MAI) was purchased from Greatcell Solar (Queanbeyan, Australia). $PC_{60}BM$ (> 99.5%) was purchased from American Dye Source (Quebec, Canada). All purchased materials were used without further purification.

2.2 SYNTHESIS AND CHARACTERIZATION OF EDOT-MeCl MONOMERS

The experimental details were applied from previous studies with some modification[29]. 3,4-dimethoxythiophene (5 g), 3-chloro-1,2-propanediol (12 g), PTSA (0.676 g), toluene (118 mL) were added into a three-neck flask. The system was purged with N_2 flow for 30 min and stirred vigorously at 95 °C under N_2 protection for 24 h. After removing of toluene under reduced pressure, the residue was purified by column chromatography (silica gel, hexane/DCM = 8/2 v/v) to give the yellowish transparent oil product, 2-(chloromethyl)-2,3-dihydrothieno[3,4-b][1,4]dioxine (EDOT-MeCl). The product was characterized by Burker AVance 300 nuclear magnetic resonance (NMR). ^{1}H NMR (300 MHz, $CDCl_3$, ppm): δ 6.19 (s, 2H, Th), 4.42-4.14 (m, 3H, -O-CH_2-CH-O-), and 3.65-3.78 (m, 2H, -CH_2-Cl).

2.3 SYNTHESIS AND CHARACTERIZATION OF PEDOT-MeCl:PSS CONDUCTING POLYMERS

PEDOT-MeCl:PSS was synthesized by the oxidative chemical polymerization method. Briefly, PSSH (3.333 g, 3.262 mmol) was dissolved in deionized (DI) water (6 - 20 ml). EDOT-MeCl (0.1341g, 0.3515 mmol) was added into the PSSH solution and stirred vigorously for 10 min to form an emulsion. Then, $Na_2S_2O_8$ (0.75 g, 3.144 mmol) and $Fe_2(SO_4)_3$ (5.6 mg, 0.01467 mmol) dissolved in 2.5 and 1 mL DI water, respectively, were dropwise added to the stirred emulsion. In 10 min later, NaOH (0- 65.24 mg, 0-1.631 mmol) dissolved in 1 mL DI water was added to the emulsion. The emulsion was stirred vigorously at 45℃ for 5-24 h until the UV-Vis absorption intensity of the solution did not change. UV-Vis absorption spectra were collected using a Varian Cary 5000 UV-Vis-NIR spectrophotometer from 200 to 1500 nm by diluting 60 µL sample with 3.5 mL DI water. EWATIT MP 62 anion exchanger (6.5 g) and LEWATIT MonoPlus S 108H cation exchanger (4.5 g) resins were added into the solution, stirred for 2 h, and removed by vacuum filtration. The product solution was in dark green color. The product was centrifuged twice at 10,000 rpm for 10 min to get rid of precipitates.

2.4 FABRICATION AND CHARACTERIZATION OF PEDOT:MeCl:PSS THIN FILMS

Glass substrates were cut into 15 mm × 15 mm pieces, and cleaned sequentially by sonication in soapy DI water, DI water, acetone, and isopropanol for 15 min each and then treated with 100 W oxygen plasma for 10 min. PEDOT-MeCl:PSS or PEDOT:PSS (100 µL) filtered through a 0.45 µm nylon filter was spin-coated onto a cleaned glass substrate at 5000 rpm for 60 s. For ambient-annealed samples, the substrates were transferred onto a hotplate and annealed at 120℃ for 25 min. For solvent-annealed samples, the substrates were transferred onto a hotplate, a drop of 200

μL toluene was added inside the Petri dish, and then the substrates were annealed inside the covered Petri dish at 120℃ for 25 min.

X-ray photoelectron spectroscopy (XPS) measurements were conducted using Kratos AXIS Ultra DLD X-ray photoelectron spectrometer to investigate the surface elements and chemical states of PEDOT-MeCl:PSS thin films annealed in ambient and solvent-vapor conditions. The incident x-rays were monochromatized Al Kα radiation (KE = 1486.6 eV) operated at 10 mA and 15 kV. All XPS data were acquired at a nominal photoelectron takeoff angle of 0º with a charge neutralizer. The survey and detailed spectra were acquired with the data point spacing of 1.0 and 0.3 eV/step, respectively, at a spectrometer pass energy of 80 eV. The high-resolution spectra were acquired with the data point spacing of 0.1 eV/step at a spectrometer pass energy of 20 eV. Data analysis was performed using CasaXPS software version 2.3.15. The binding energy scale was calibrated by assigning the lowest binding energy C1s peak to 284.8 eV. Raman Spectroscopy measurements were carried out on a Thermo Scientific DXR2 Raman Microscope to investigate the chemical structure of PEDOT-MeCl:PSS and PEDOT:PSS. A 532 nm green laser with the laser power between 1-5 mW was illuminated and focused through a 50x objective lens onto the polymer thin films. Raman spectra were fitted using PeakFit with assumption of 50% Gaussian and 50% Lorentzian component peaks. Contact angles were measured using First Ten Angstroms FTA-100 contact angle and surface tension instrument to investigate the surface hydrophobicity. Tapping-mode atomic force microscope (TM-AFM) measurements were performed on a Digital Multimode AFM equipped with a Nanoscope IVa controller to study the film morphologies. PEDOT-MeCl:PSS film thicknesses were measured using Olympus-OLS41 profilometer.

2.5 FABRICATION AND CHARACTERIZATION OF $MAPbI_3$ PEROVSKITE THIN FILMS

Indium-tin oxide (ITO) coated glass (10 ohm sq^{-1}, Colorado Concept Coatings, LLC) was cut into 15 mm × 15 mm pieces, which were then cleaned following the steps described above for the cleaning of glass substrates. The PEDOT-MeCl:PSS or PEDOT:PSS thin films were prepared under annealing in ambient or toluene vapor as described above and the substrates were transferred into N_2 glove box for making $MAPbI_3$ perovskite films. The $MAPbI_3$ perovskite precursor solutions were prepared by dissolving MAI and PbI_2 at a 1:1 molar ratio in GBL and DMSO (7:3, v:v) with a total concentration of 2.0 M. The precursor was mixed at 70℃ for 2 h and was filtered through a 0.45 μm PTFE filter before use. A 70 μL drop of precursor solution was spin-coated on a cleaned substrate at 1000 rpm for 15 s, and 4000 rpm for 45 s in a nitrogen glove box. 500 μL toluene anti-solvent was *in situ* dripped onto the substrate during the last 15 s of the second spin-coating step. The $MAPbI_3$ perovskite films were then thermally annealed at 100℃ for 10 min. Scanning electronic microscope (SEM) images were acquired using a FEI Sirion SEM operated at 5 kV to determine the surface morphology of $MAPbI_3$ perovskite thin films. Two-dimensional XRD patterns were collected with Burker GADDS D8 Focus Powder Discover diffractometer using Cu Kα radiation (λ = 1.5419 Å) and the data were processed using the EVA package provided by Burker Axs to investigate the crystalline structures of $MAPbI_3$ perovskite thin films. UV-vis absorption spectra were collected using a Varian Cary 5000 UV-vis-NIR spectrophotometer. The time-resolved photoluminescence (TRPL) measurements were taken by Flou Time 100 spectrometer by means of Time-Correlated Single Photon Counting (TSCPC). A 470 nm laser with the pulse width of 70 – 90 ps was excited from the glass side and the TRPL decays were measured at the peak emission wavelength (780 nm).

2.6 FABRICATION AND CHARACTERIZATION OF $MAPbI_3$ PEROVSKITE SOLAR CELLS

The ITO/PEDOT-MeCl:PSS (or PEDOT:PSS)/$MAPbI_3$ films were fabricated as described above. A $PC_{60}BM$ solution (15 mg mL^{-1} in chloroform) was then spin coated on the perovskite films at 4000 rpm for 60 s and dried without annealing. Then a BCP solution (2 mg mL^{-1} in 2-propanol) was spin coated on the $PC_{60}BM$ films at 4000 rpm for 60 s and dried without annealing. Finally, sixteen silver electrodes with thickness of 150 nm and areas of 3.14×10^{-6} m^2 were thermally evaporated on each substrate through a shadow mask at the background pressure < 10^{-6} torr. The resulting device structure is ITO/PEDOT-MeCl:PSS/$MAPbI_3$/$PC_{60}BM$/BCP/Ag.

The current density-voltage (J-V) characteristic curves were measured in a N_2 glove box with a Keithley 2400 Source Meter and a solar simulator with a Solar Light Co. Xenon lamp (16S-300W) and an AM 1.5 filter. The light intensity was calibrated to 100 mW cm^{-2} using a calibrated silicon solar cell that had been previously standardized at the National Renewable Energy Laboratory.

Chapter 3. RESULTS AND DISCUSSION

3.1 OXIDATIVE CHEMICAL POLYMERIZATION OF EDOT-MeCl

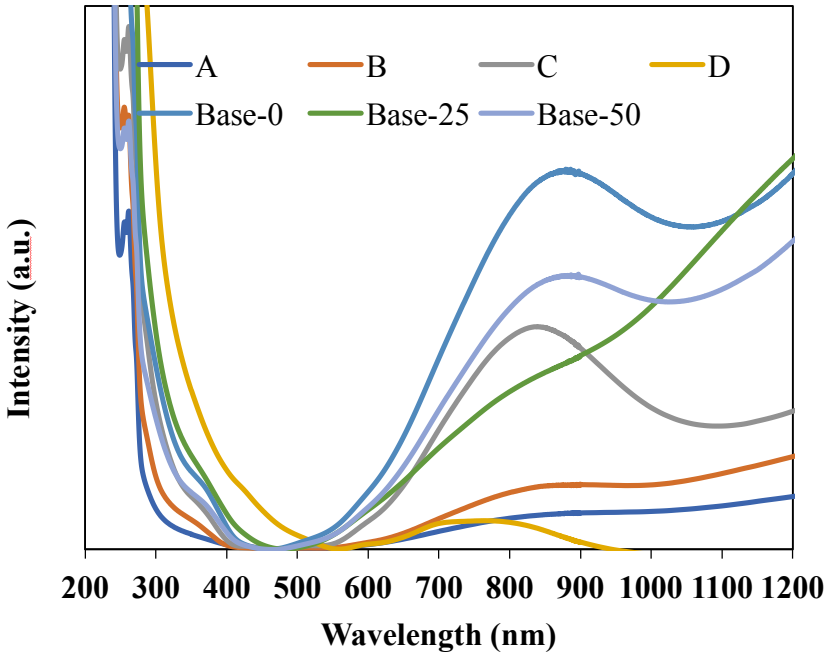

Figure 3-1. UV-Vis spectra of PEDOT-MeCl:PSS solutions synthesized under different polymerization conditions summarized in Table 1. Spectra were taken after ion exchanging. The reaction time is 24h for samples A-D, 5h for Base-0, 23h for Base-25, and 6h for Base-50. Spectra are normalized by matching the lowest absorption point.

The oxidative chemical polymerization of EDOT-MeCl in the presence of PSSH is illustrated in Scheme 1, which is adopted from the oxidative polymerization of PEDOT:PSS. Sodium persulfate ($Na_2S_2O_8$) has been used as a peroxidic oxidants for EDOT to form conductive PEDOT:PSS complex[30]. Small amount of $Fe_2(SO_4)_3$ is added to the reaction mixture to control the catalytic decomposition of sodium persulfate at certain rates in order to yield high and reproducible conductivity of the PEDOT:PSS complex. From the stoichiometric point of view, one equivalent

of peroxydisulfate is needed for each thiophene unit taking two electrons from each thiophene. Additional peroxodisulfate is consumed in the oxidation of the polymer chain resulting in a polycation. The EDOT monomers will disperse into the hydrophobic environment inside PSS shell, and oxidized by ferric ion. Persulfate is used to oxidized ferrous ions produced during the reaction. The PEDOT will be positively charges in every three units, and will be doped by PSS. At the beginning, as shown in **Table 3-1**, we tried to oxidize EDOT-MeCl with the same amount of oxidant as EDOT, but is was found that EDOT-MeCl could not be oxidized by oxidant under the same condition, which can be proved by their UV-vis spectra in **Figure 3-1**. The reason behind is because of the high electronegativity of the –MeCl group, which makes the EDOT-MeCl monomer harder to diffuse into PSSH micelles than EDOT monomer. As shown in **Figure 3-1**, both polaron and biolaron peaks increased with the increasing amount of oxidant, however, when four times of oxidant was added into the solution, both polaron and bipolaron decreased significantly, and the solution presented a greyish-green color with peculiar odor. In this case, the monomer has been over-oxidized. Thus, it can be seen that three times the amount of oxidant is the most suitable oxidant for EDOT-MeCl in its oxidation reaction.

Temperature is another important parameter for the EDOT-MeCl polymerization. For EDOT-MeCl, the melting point is 39-44 ℃. At room temperature, it is a yellowish solid and insoluble in water. Therefore, room temperature polymerization occurs slowly than EDOT, and most monomers do not participate in the reaction, but accumulate at the bottom of the reactor as precipitates. Because of the good thermal stability of PEDOT-MeCl, we increased the reaction temperature to 45℃ to ensure that all monomers are liquid at this temperature. According to the UV-vis spectra shown in **Figure 3-1**, the heating treatment obviously increased the intensity of both polaron and bipolaron peak, making the polymer more effectively oxidize and doped. The

increase of temperature accelerates the thermal motion of molecules, thus increases the rate of collision between particles, which finally increases the reaction rate. In addition, the liquid – liquid mass transfer rate is much higher that the solid – liquid mass transfer. Another purpose of increasing temperature is to improve the solubility of EDOT-MeCl in water in the presence of PSS. So, the reaction temperature was set at 45℃.

Sulfonic acids typically have a low pKa value. For example, the pKa of benzenesulfonic acid is 0.70[30]. The reaction mixture turns more acidic as the reaction progresses since each mole of EDOT-Cl releases two moles of protons. The rising acidity increases the difficulty of PSS dissociation, which hinders the doping of oxidized, positively charged PEDOT-MeCl. Besides, the strong acidity of PEDOT:PSS is the main reason for the instability in perovskite solar cells[31]. If we release the PSS ion by adding a few sodium hydroxides, things will be different in the reaction. In this case, ferric ion is more likely to be attracted by PSS because of electrostatic force, so the selectivity of this reaction will be higher than that without NaOH. Because of the high electron affinity, this function group will be gathered around by electron, which makes it even harder to get itself inside the PSS shell. Besides, the oxidizing ability will be weakened in an alkaline environment, so it takes a longer time to react. As shown in **Table 3-1**, we added 0% (Base-0), 25% (Base-25) and 50% (Base-50) molar ratio of NaOH into the solution while polymerization, and all of them have better polaron and bipolaron absorption than other samples. However, when we increase the molar ration of NaOH to 75%, what we end up with is a grey-green suspension, which is different from what we would expect from a conductive polymer. Therefore, in the following discussion, we only study the properties of three samples.

Table 3-1. Summary of the molar ratios of reactants, the volume of total DI water, reaction temperature for the polymerization of PEDOT-MeCl:PSS and the product color. The molar ratio of PSSH:EDOT-MeCl was fixed at 4.64.

Sample Name	NaOH:PSSH	$Na_2S_2O_8$: EDOT-MeCl	$Fe_2(SO_4)_3$: EDOT-MeCl	DI H_2O (mL)	Temperature (°C)	Product Color
A	0	1.49	0.006	24	RT	Yellow
B	0	2.98	0.012	24	RT	Green
C	0	4.47	0.0201	24	RT	Dark green
D	0	5.96	0.0268	24	RT	Grey-green
Base-0	0	4.47	0.0201	10.5	45	Dark green
Base-25	0.25	4.47	0.0201	10.5	45	Dark green
Base-50	0.5	4.47	0.0201	10.5	45	Dark green

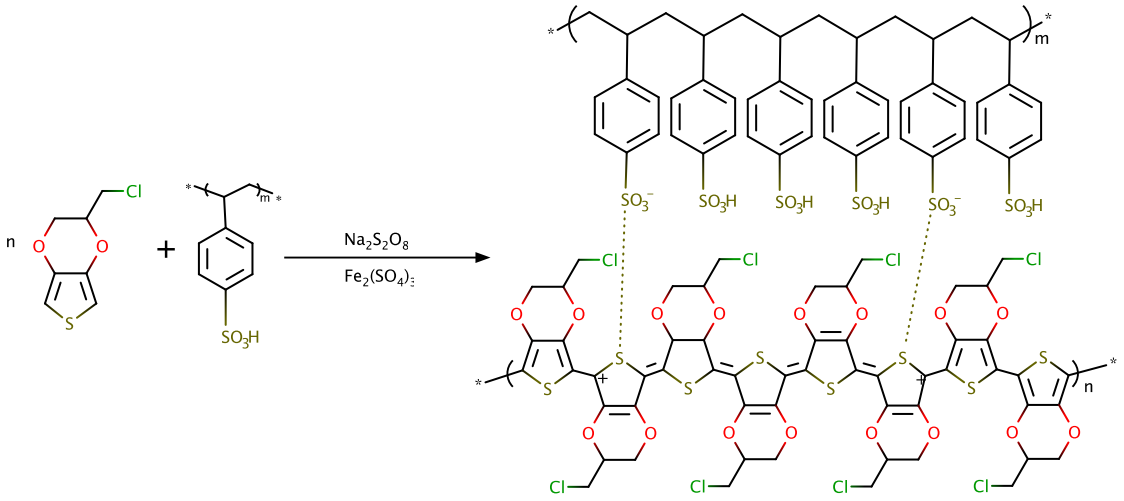

Scheme 3-1. Oxidative chemical polymerization of EDOT-MeCl in the presence of PSSH.

During the reaction, the PEDOT-MeCl can be neutralized not only by PSS ion but also by sulfuric acid ions. PEDOT-MeCl is insoluble in water, and PSS ion keeps it stable in water. If it is doped by sulfate ion, the polymer cannot by dissolved in water and remains stable, so a precipitate is formed.

It is known that there may be three redox states, namely PEDOT-$MeCl^{2+}$(bipolaron), PEDOT-$MeCl^{+}$ (polaron) and PEDOT-MeCl (neutral) in PEDOT-MeCl (**Figure 3-2**). These three states of PEDOT-MeCl chains show adsorption at different wavelength: the neutral polymer chains show absorption around 600 nm, the chains in polaron state show absorption around 800 nm and the chains in bipolaron state show broad absorption in the infrared region (IR, > 1200 nm). The UV-vis-NIR spectra change over time of Base-0 sample are shown in **Figure 3-3a**. At the beginning of the reaction, there is no polaronic or bipolaronic state produced in the solution. As the reaction went on, both polaron and bipolaron pkeaks appeared at the same time, and with the passage of time, the intensity became higher simultaneously. It can be inferred that, at the same time as the polymerization reaction takes place, the polymer is also being oxidized to polaronic and bipolaronic states. After 5 hours of reaction, it can be seen from the absorption spectrum that the spectral line at this time almost coincides with the 4.5-hour line has no obvious change compared with the 4-hour line. Based on this phenomenon, we can judge that the reaction has reached the end point.

The reaction kinetics was investigated by taking dynamic UV-vis-NIR spectra of Base-0 and Base-50. As previously described, we used the same method to record the UV-vis spectra of Base-50 over time, and polaron and bipolaron peak intensity change with time was plotted into **Figure 3-3b**. It can be seen from this figure that, for Base-0 sample, both polaron and bipolaron peak increased rapidly within the first three hours of the reaction, and then reached plateau at the same point. When we added 50% NaOH to the system, it can be observed from the figure that the growth rate of both polaron and bipolaron peaks has slowed down. After 5 hours of reaction, the growth curves of the two peaks tended to be stable. This phenomenon proves that, as we mentioned before, after the addition of NaOH to the reactants, the rate of polymerization becomes slower and the

time required for the reaction becomes longer. We attributed this to the fact that NaOH weakens the oxidizing power of $Fe_2(SO_4)_3$. In this reaction, a slower reaction rate allows PEDOT-MeCl to be better doped by PSS^-, rather than being doped by small molecules of sulfate and forming precipitation.

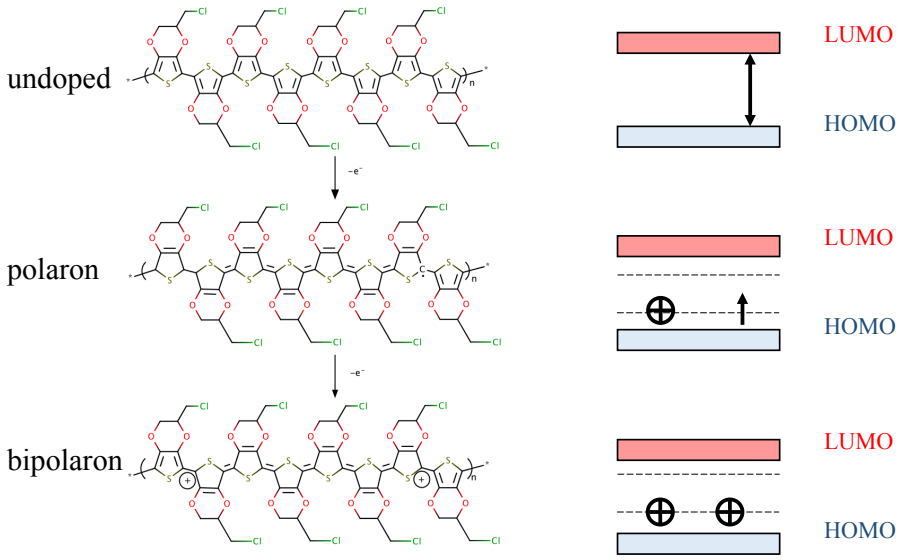

Figure 3-2. (Left) Schematic for p-doping of PEDOT-MeCl and (right) the corresponding band structure evolution: electron transfer (-e-) to the undoped polymer (top) leads to the formation of a polaron (middle) and finally a bipolaron state (bottom)

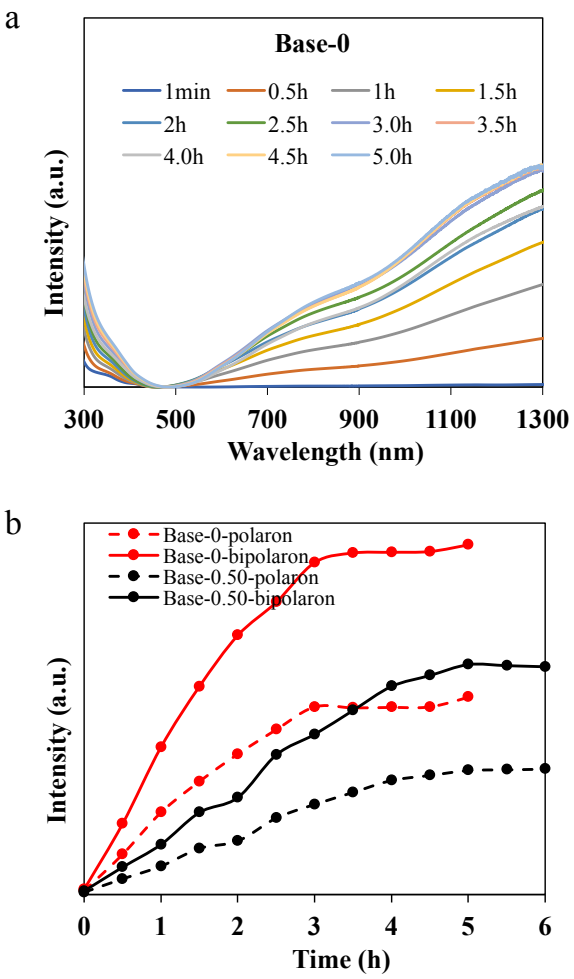

Figure 3-3. (a) UV-Vis spectra of PEDOT-MeCl:PSS solutions obtained under different polymerization conditions summarized in Table 1. Spectra are normalized by matching the lowest absorption point. (b) Time-depend UV-Vis spectra for sample Baso-0. (c) Peak intensity of polaron and biopolaron absorption as a function of reaction time for samples Base-0, Base-25 and Base-50.

3.2 PEDOT-MeCl:PSS ANNEALED IN AIR AND SOLVENT VAPOR ENVIRONMENT

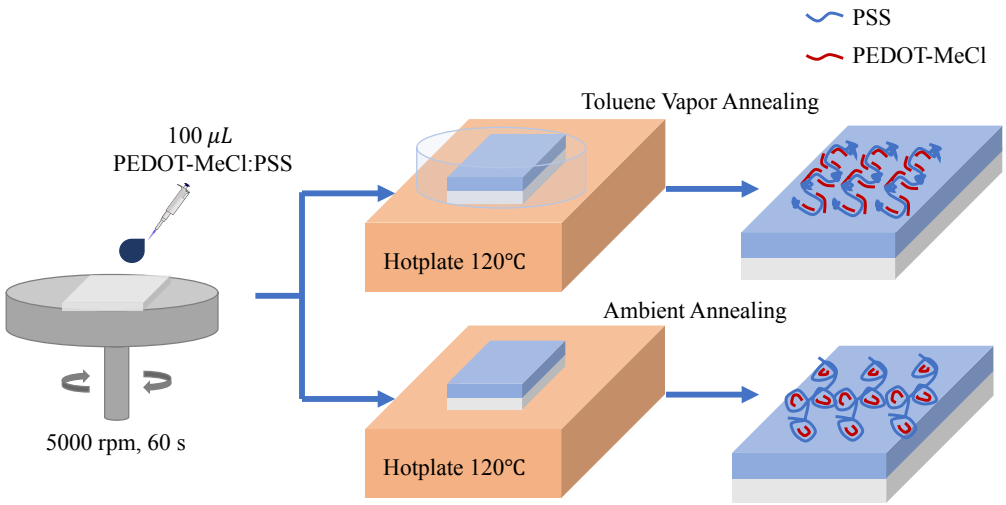

Figure 3-4. Schematics of preparing PEDOT-MeCl:PSS thin films with toluene vapor annealing and ambient annealing as well as the possible resulted surface morphology of PEDOT-MeCl:PSS.

As mentioned previously, PSSH is isolated in water and therefore greatly affects the conductivity of PEDOT-MeCl:PSS. In previous studies, additives as secondary dopants have been used to increase the conductivity of PEDOT:PSS. Sulfoxides, such as dimethyl sulfoxide (DMSO), and polyols, such ethylene glycol (EG), are the most popular secondary dopants with the highest conductivity that currently obtained. It has been found that the film forming process is the critical step for these secondary dopants to come into effect[32]. When PEDOT:PSS is deposited from aqueous dispersion, it does not reach an equilibrium state in the solid film. Instead it is "frozen" in a non-equilibrium state. The presence of the high-boiling solvent with a low dielectric constant allows the blend to rearrange[33, 34], which means that the PEDOT:PSS chromophores find a new thermodynamically preferable position that is not identical to that obtained in the processing and drying from the aqueous system. This principle can be applied to PEDOT-MeCl:PSS films as well. As shown in **Figure 3-4**, instead of using a secondary dopant, we used a solvent vapor annealing method to anneal the PEDOT-MeCl:PSS film in a toluene vapor environment. The hypothesis is, in the hydrophobic environment, more hydrophobic groups, PEDOT-MeCl, will accumulate on the surface, and the amount of PSS will decrease on the surface compared to annealing in air. Therefore, it will achieve the purpose of rearrangement.

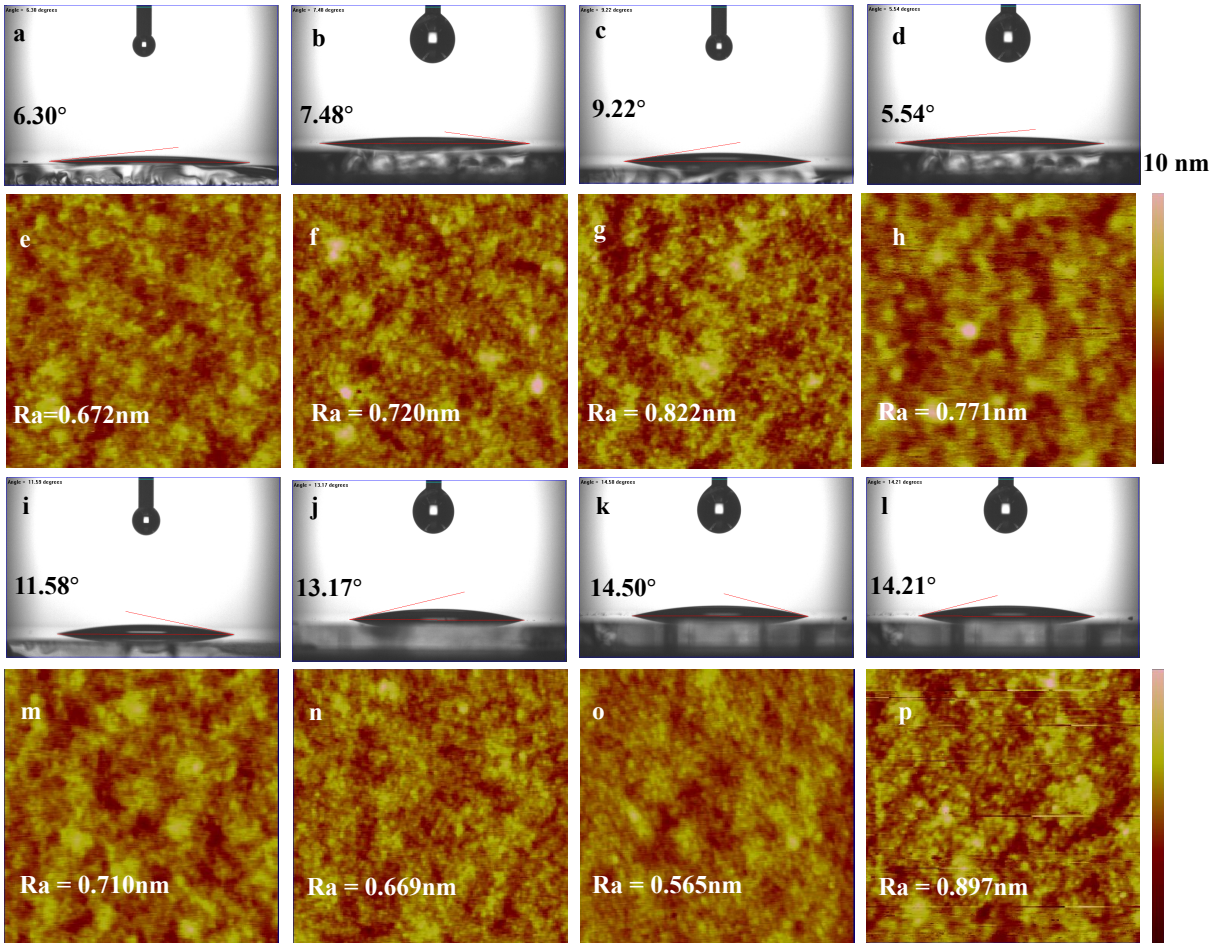

Figure 3-5. Contact angle measurements and AFM images. a, b, c, d are contacting angle images for PEDOT:PSS, Base-0, Base-25, Base-50 prepared in ambient environment, respectively. i, j, k, l are contacting angle images for PEDOT:PSS, Base-0, Base-25, Base-50 prepared in toluene vapor environment, respectively. e, f, g, h are AFM images for PEDPT:PSS, Base-0, Base-25, Base-50 prepared in ambient environment, respectively. m, n, o, p are AFM images for PEDOT:PSS, Base-0, Base-25, Base-50 prepared in toluene vapor environment, respectively. Z-scale bar is 10 nm.

Given the readily rearrange of PEDOT-MeCl and PSS, static contact angle measurements were conducted and corresponding images of the water droplets on the PEDOT:PSS and PEDOT-

MeCl:PSS surfaces are illustrated in **Fig 3-5**. PEDOT-MeCl:PSS films exhibited a larger contact angle before and after solvent annealing, suggesting that PEDOT-MeCl:PSS films are more hydrophobic than PEDOT:PSS films. Moreover, distinct changes in contact angle were observed, for not only PEDOT:PSS but also PEDOT-MeCl:PSS, indicating that there are distinct phase changes occurred in the PEDOT:PSS and PEDOT-MeCl:PSS films during annealing. A more hydrophobic and dense surface has been reported to lead to a larger perovskite crystal size [35] and enhance the waterproofness and operational lifetime of optoelectronic devices[36].

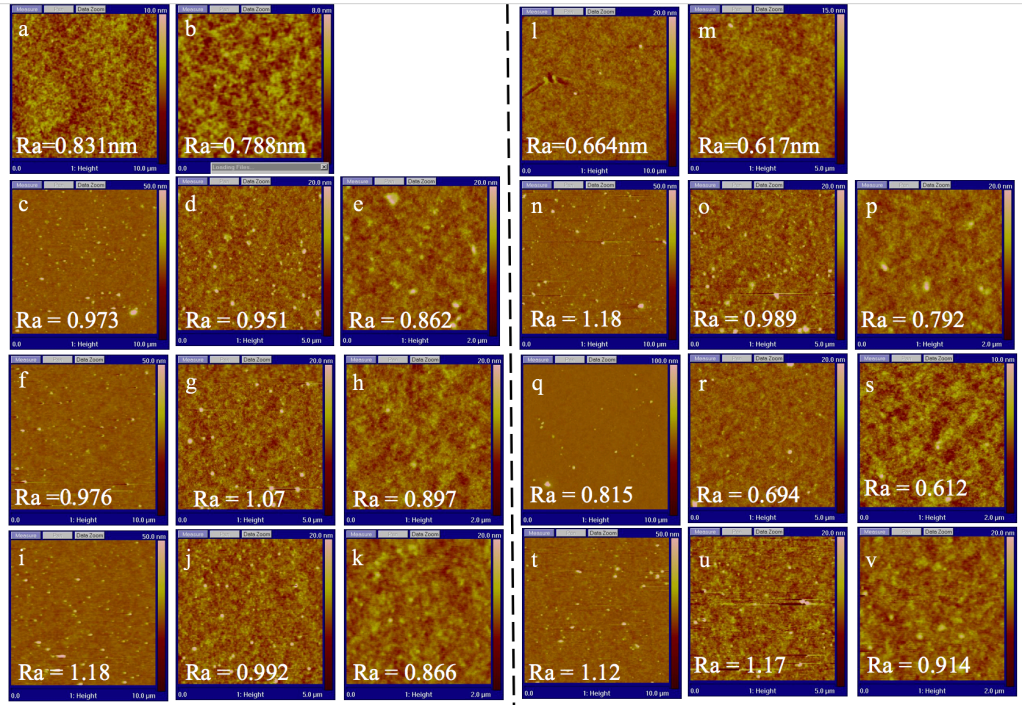

Figure 3-6. Topographic AFM images of the thin films of PEDOT:PSS (a, b, l, m) and PEDOT-MeCl:PSS synthesized with the NaOH:PSSH molar ratio of 0 (c - e, n - p), 0.25 (f - h, q - s), 0.5 (i - k, t - v) under ambient (a - k) and toluene vapor annealing (l - v) . image sizes are 10 μm × 10 μm for (a, c, f, i, l, n, q, t), 5 μm × 5 μm for (b, d, g, j, m, o, r, u), and 2 μm ×2 μm for (e, h, k, p, s, v)

In addition, the AFM images for each sample are listed in **Figure 3-5** below its contacting angle image and **Figure 3-6** to investigate the surface morphology changes of these films. **Figure 3-5** e, f, g, h are topography images PEDOT:PSS and PEDOT-MeCl:PSS images annealed in are and **Figure 3-5** m, n, o, p are topography images for PEDOT:PSS and PEDOT-MeCl:PSS annealed in toluene vapor environment, respectively. for As shown, PEDOT:PSS and PEDOT-MeCl:PSS have a comparable surface morphology and roughness prepared in not only air annealing condition but also solvent annealing condition, while the solvent annealed films have a different morphology and a slightly change of roughness. For PEDOT:PSS, the roughness increased from 0.672 nm to 0.710 nm after solvent annealing, and for Base-50, the roughness increased from 0.771 nm to 0.897 nm. However, films in Base-0 and Base-25 samples have a smaller roughness after solvent annealing. It decreased from 0.720 nm to 0.669 nm for Base-0 and 0.822 to 0.565 nm for Base-25. Meanwhile, in the topography images, grains and some elongated structures are observed on the surface of these films. In the topography image of air annealed films, grains and some elongated structures are observed on the surface. Particles can also be observed on the solvent annealed film surface, as well as some elongated features. After enlarging the image, there are small islands in the topography images of solvent annealed films, which are irregular in shape, seldom circular, and mostly elongated. The regions or islands in **Figure 3-5**, m, n, o, p, are attributed to excess PSS materials[18]. The solvent annealing method thus induces a phase separation on the nanometer scale characterized by a segregation of the excess PSS in domains surrounded by a PEDOT:PSS and PEDOT-MeCl:PSS phase.

To strength the interpretation of the AFM images, XPS measurements are performed on these films. XPS is a surface-sensitive technique, but with no lateral resolution, since the size of the analyzed spot is about a few mm[33]. Hence XPS appears complementary to AFM techniques.

Both PEDOT-MeCl and PSS contain one sulfur atom per repeat unit. The sulfur atom in PEDOT-MeCl is within the thiophene, ring whereas in PSS it is included in the sulfonate moiety. Due to those different chemical environments, the S(2p) electrons of PEDOT-MeCl and PSS have different binding energies so that the composition of PEDOT-MeCl:PSS can be can be analyzed by XPS. The XPS spectrum displays two contributions (see **Figure 3-7**). The sulfur signal for PSS appears at higher binding energy (168 – 169 eV) due to the three electronegative oxygen atoms withdrawing the electron density of sulfur atom. The S(2p) doublet at 164 – 165 eV comes from PEDOT-MeCl. Upon using solvent annealing method, the amount of PEDOT-MeCl is almost not changed. Note that similar negligible changes in the S(2p) spectra of PEDOT:PSS upon the addition of a secondary dopant have also been observed by others[33, 37]. To shed light on the relationship between the composition and the morphology of PEDOT-MeCl:PSS, the XPS wide scan has been performed. As shown in **Table 3-2**, the concentration of Cl element has been increased after solvent annealing, which indicate that there're more PEDOT-MeCl exposed on the surface after treatment. As stated above, this is due to the occurrence of a phase separation on the sample surface.

Table 3-2. XPS atomic percentage of Base-50 PEDOT-MeCl:PSS films annealed in ambient and in solvent toluene vapor.

	C(1s)	O(1s)	Na(1s)	S(2p)	Cl(2p)
Base-50-air	63.9	22.6	6.4	5.9	1.2
Base-50-sol	65.4	21.7	6.0	5.4	1.5

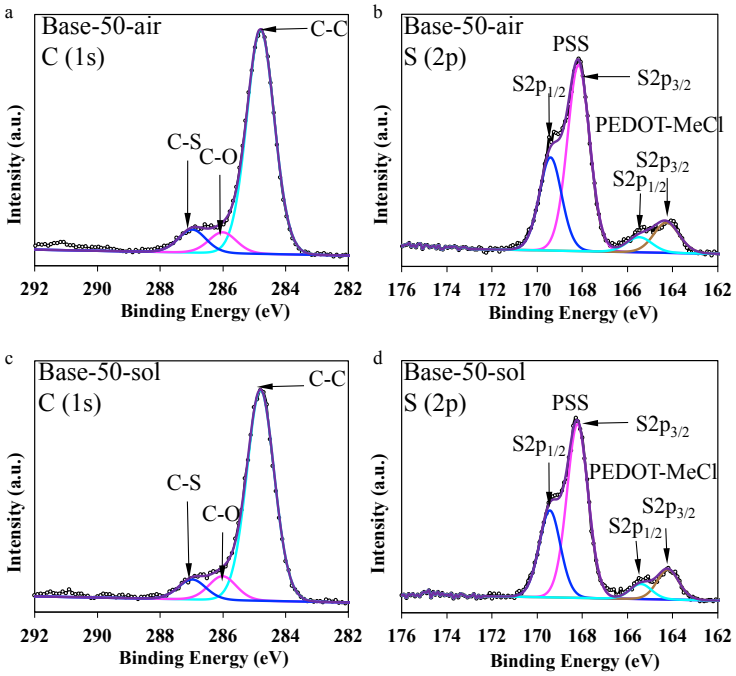

Figure 3-7. a C(1s) peak of XPS spectra of Base-50-air, b S(2p) peak of XPS spectra of Base-50-air, c C(1s) peak of XPS spectra of Base-50-sol, d S(2p) peak of XPS spectra of Base-50-sol.

Since Raman spectra can show the chemical structure of polymers, the effect of the solvent annealing will be supported by Raman spectra. Raman spectra (532 nm excitation line) of PEDOT:PSS and selected PEDOT-MeCl:PSS samples for which the surface morphological and elemental analysis have also been carried out, were recorded between 1300 and 1700 cm^{-2} and shown in **Fig 3-7**. The most intense peak centered at around 1437 cm^{-1} is assigned to the $C_\alpha = C_\beta$ symmetric stretching vibration. The two other bands at around 1504 cm^{-1} and 1570 cm^{-1} correspond to the $C_\alpha = C_\beta$ asymmetric stretching vibrations[38]. The inconspicuous peak centered at around 1534 cm^{-1} arises from the splitting of the asymmetric vibrations. The other peak observed at around 1361 cm^{-1} was assigned to $C_\beta - C'_\beta$ vibration[39]. The $C_\beta - C'_\beta$ peak as well as $C_\alpha = C_\beta$ symmetrical stretching vibration peak were blue shifted when introducing the chloromethyl

function group to EDOT, that is because the electronegativity of chloromethyl group is higher than EDOT, the electron density around the EDOT decreases and the binding energy increases, so that these peaks shifts positively. From the curve-fit result of Raman spectrum, it is clearly seen that the most intense peak, assigned to the symmetric $C_\alpha = C_\beta$ stretching vibration, is a combination of two separate bands, one of which is due to the symmetric $C_\alpha = C_\beta$ stretching vibration from the PEDOT segments involving the benzoid structure (centered at 1421 cm^{-1} for PEDOT:PSS and 1424 cm^{-1} for PEDOT-MeCl:PSS) and the other is due to the quinoid structure (centered at 1442 cm^{-1} for PEDOT:PSS and 1444 cm^{-1} for PEDOT-MeCl)[40]. For not only PEDOT:PSS, but also PEDOT-MeCl:PSS, the $C_\alpha = C_\beta$ symmetrical stretching vibration peaks were broadened and became more intense after solvent annealing, comparing that with ambient annealed samples. These spectral changes in PEDOT:PSS and PEDOT-MeCl:PSS are correlated with the change in the conformation of the PEDOT or PEDOT-MeCl chains from a benzoid structure to a quinoid structure. It is obvious that the ratio of the integrated intensities of the two bands (quinoid: benzoid) becomes larger as the doping level increases. As shown in **table 3-2**, the quiniod to benzoid ratio (Q/B) of PEDOT:PSS has been increased from 1.8 to 3.4 after solvent annealing. For Base-0, the ratio increases from 2.1 to 2.6 after solvent annealing, and it increases from 2.2 to 4.3 for Base-25 and 1.8 to 3.4 for Base-50 after solvent annealing. We can interpret the change observed in Raman spectra as a change from benzoid structure toward a quinoid structure of the PEDOT-MeCl molecules due to a move from a coil structure toward an extended coil or linear structure of PEDOT-MeCl chains[41-43]. Ouyang *et al.*[44] proposed that the benzoid and quinoid structure of PEDOT chains corresponds to the coiled conformation and expanded-coil or liner conformation, respectively. The expanded-coil conformation retains the two PEDOT rings in the same plane to facilitate the $\pi -$ electron delocalization to cause increase in the conductivity of the PEDOT

film[45]. Hence, we presume that the solvent-annealing method not only induced phase separation but also enhanced the hole mobility in the PEDOT or PEDOT-MeCl:PSS films.

Table 3-3. The ratio of quinoid to benzoid structures in Al 4083 PEDOT:PSS and three different PEDOT-MeCl:PSS films prepared under ambient and toluene vapor annealing. The ratios were estimated from the peak area ratios corresponding to the symmetric $\boldsymbol{C_\alpha = C_\beta}$ vibrational mode at 1444 cm-1 for quinoid and at 1424 cm-1 for benzoid structured PEDOT-MeCl backbone.

Films	Al 4083		Base-0		Base-25		Base-50	
	Air	Sol	Air	Sol	Air	Sol	Air	Sol
Quinoid/Benzoid	1.8	3.4	2.1	2.6	2.2	4.3	1.8	3.4

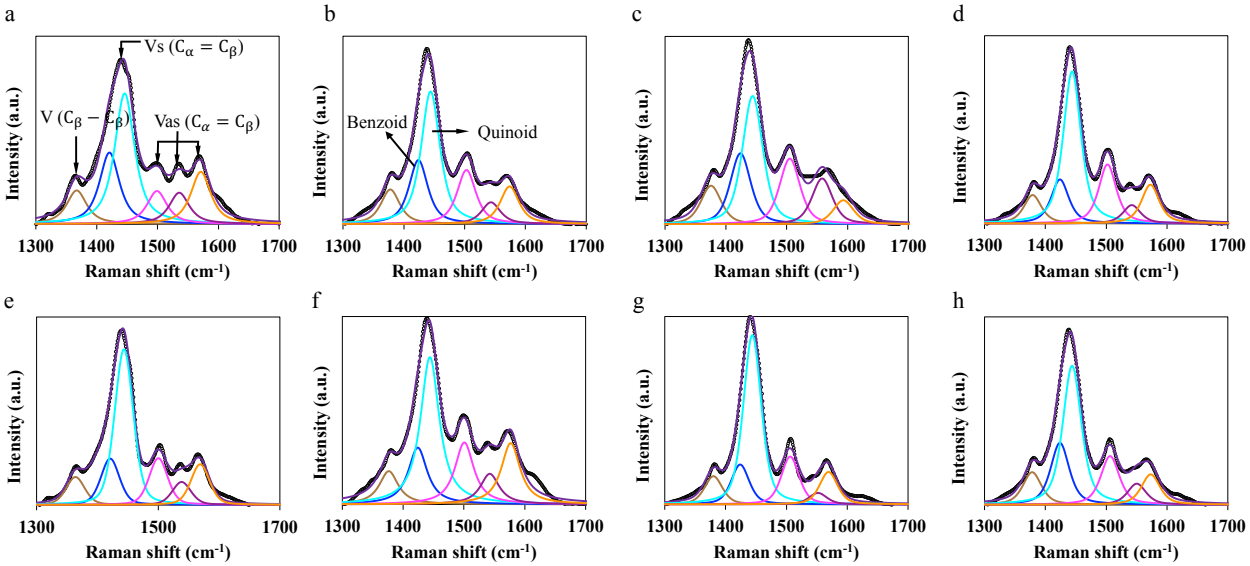

Figure 3-8. Raman spectra for PEDOT:PSS and PEDOT-MeCl:PSS. a, b, c, d, Raman spectra of PEDOT:PSS, Base-0, Base-25 and Base-50 annelaed in ambient environment, respectively. e, f, g, h, Raman spectra of PEDOT:PSS, Base-0, Base-25 and Base-50 annealed in toluene vapor environment, respectively.

3.3 $MAPbI_3$ PEROVSKITE FILMS ON PEDOT-MeCl:PSS

We used the one-step solution process[46] with anti-solvent wash to synthesize dense, pinhole-free $MAPbI_3$ perovskite thin films on PEDOT:PSS and PEDOT-MeCl:PSS films annealed in air and toluene vapor conditions. All precursors (MAI and PbI_2) were dissolved in a DMSO:GBL (3:7, v/v) co-solvent to a total concentration of 2.0 M. During spin coating, the anti-solvent wash with 500 μL toluene was performed to remove excess DMSO from the complex PbI_2·2DMSO to result in the rapid formation of A-PbI_2-DMSO intermediates. All the films were annealed at 100℃ for 10 min to remove complexed DMSO under a controlled reaction of the metal and cation during the annealing step, creating homogeneous, densely packed perovskite films with clear grain boundaries. Clearly, the SEM images in Fig. 7 show that the $MAPbI_3$ films prepared on PEDOT-MeCl:PSS and PEDOT:PSS annealed in toluene vapor produced larger grains than those on PEDOT-MeCl:PSS and PEDOT:PSS annealed in air.

The top-view SEM images of the $MAPbI_3$ films on PEDOT:PSS and PEDOT-MeCl:PSS films annealed in air and toluene vapor conditions shown in **Figure 3-9** reveal a clear correlation between the substrate surface wetting capability and the grain morphology. First, the average grain size is much larger for $MAPbI_3$ films on hydrophobic surfaces. The sizes of $MAPbI_3$ grains on air-annealed PEDOT:PSS (45 nm), Base-0 (50 nm), Base-25 (60nm), Base-50 (80nm) are smaller than solvent vapor-annealed PEDOT:PSS (200 nm), Base-0 (200 nm), Base-25 (220 nm), Base-50 (90 nm). This could be due to the higher amount of PEDOT/PEDOT-MeCl exposed on the surface decreased the surface wettability, thus a non-wetting surface has been produced after solvent annealing. Previous results have shown that, the surface tension dragging force from the wetting substrates will reduce the grain boundary mobility, which will dramatically diminish if the substrate is non-wetting and smooth, yielding a higher grain boundary mobility, which enables the

growth of larger grains[35, 47]. The very smooth surface of the HTL also suppresses the nucleation in small cavity and contributes to the high grain boundary mobility. Second, most of the MAPbI3 films have a higher quality growing on solvent-annealed HTL. A smooth, dense, and pinhole free morphology were formed for Base-0 and Base-50 annealed in air and solvent environment. this could be attributed to the stronger interaction between Pb and Cl, which helps to keep more lead fixed at the interface between HTL and $MAPbI_3$ layers. The chemical bonds formed during crystal formation give $MAPbI_3$ better stability, and therefore produce less PbI_2 on the surface. while both solvent-annealed PEDOT:PSS and Base-25 films have a few, small pinholes and even coverage. A few smaller, lighter grains appeared in the solvent-annealed PEDOT:PSS and Base-25 films, which could be due to a slight degradation.

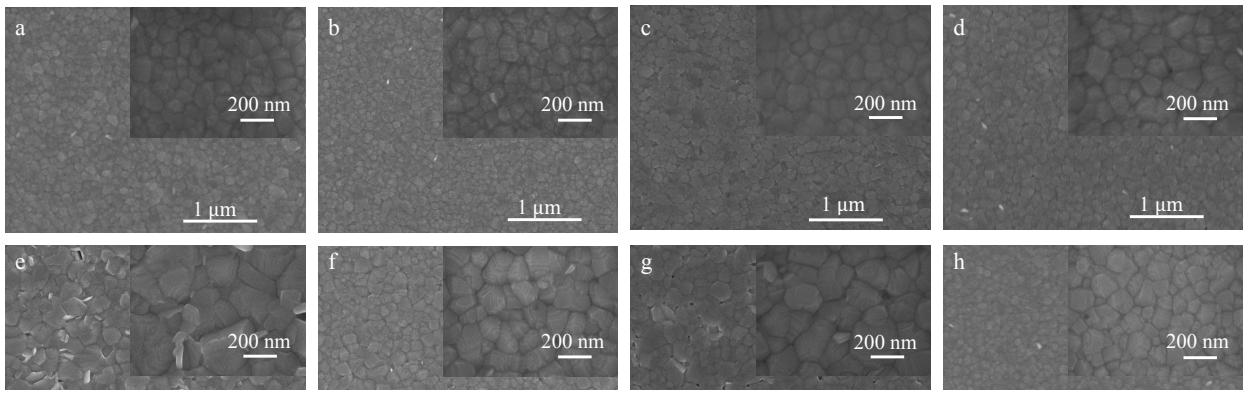

Figure 3-9. SEM images for $MAPbI_3$ films fabricated on (a) Al 4083 PEDOT:PSS and (b) Base-0, (c) Base-25, and (d) Base-50 PEDOT-MeCl:PSS annealed in air, and (e) Al 4083 PEDOT:PSS and (f) Base-0, (g) Base-25, and (h) Base-50 PEDOT-MeCl:PSS annealed in solvent toluene vapor.

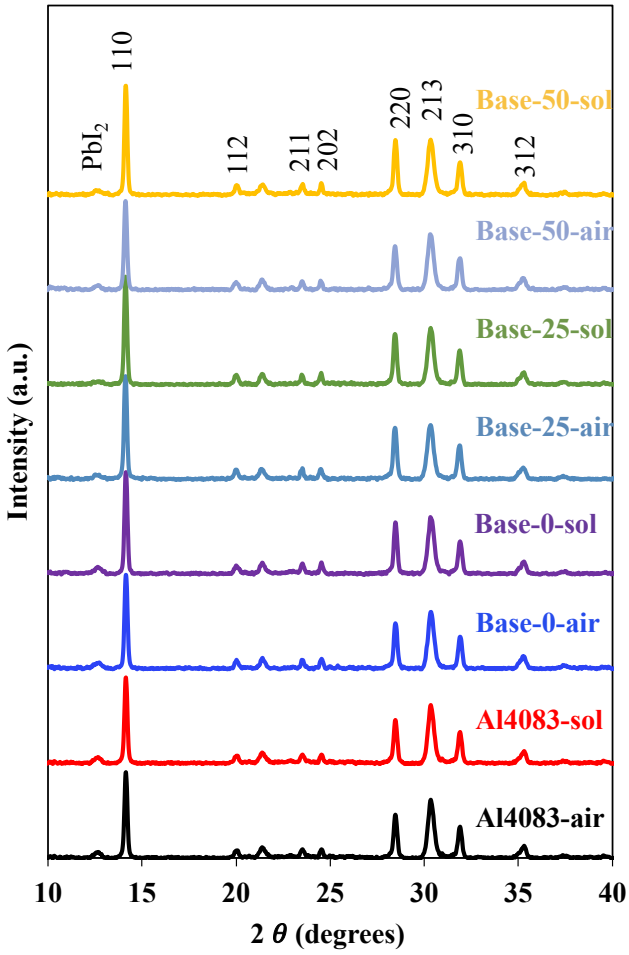

Figure 3-10. XRD patterns of $MAPbI_3$ films prepared on commercial Al 4083 PEDOT:PSS and synthesized Base-0, Base-25 and Base-50 PEDOT-MeCl:PSS films annealed in air and solvent toluene vapor.

The $MAPbI_3$ thin films were further characterized with X-ray diffraction (XRD) to determine the phase and crystallinity. As shown in **Figure 3-10**, all the samples showed intense diffraction peaks at 14.1°, 28.5°, and 31.9° which is well matched with the (110), (220), and (310) crystal facets of $MAPbI_3$, respectively. notably, the XRD peak of the $MAPbI_3$ film grown on solvent-annealed HTLs possessed a higher intensity than those formed on air-annealed PEDOT:PSS and PEDOT-MeCl:PSS, showing that both grain size and crystallinity of the $MAPbI_3$ films deposited on solvent-annealed HTLs. The ratio of the intensity of the peak at 12.85° for PbI_2

to that at 14.1° for $MAPbI_3$ (110) are shown in **Figure 3-11**. For all PEDOT-MeCl samples, the ratio of PbI_2 to $MAPbI_3$ (110) was lower than that of PEDOT samples, which means that less $MAPbI_3$ degradation happened on PEDOT-MeCl:PSS surface, indicating that the interaction between Cl and Pb can stabilize $MAPbI_3$ crystal. Noticeably, for PEDOT-MeCl samples, the ratio decreased after solvent annealing, which indicates that a higher quality of perovskite film was formed after solvent annealing, just as the SEM images showed previously. But for PEDOT samples, there're more PbI_2 exists on the surface after using solvent annealing, which explained the light regions on the SEM images.

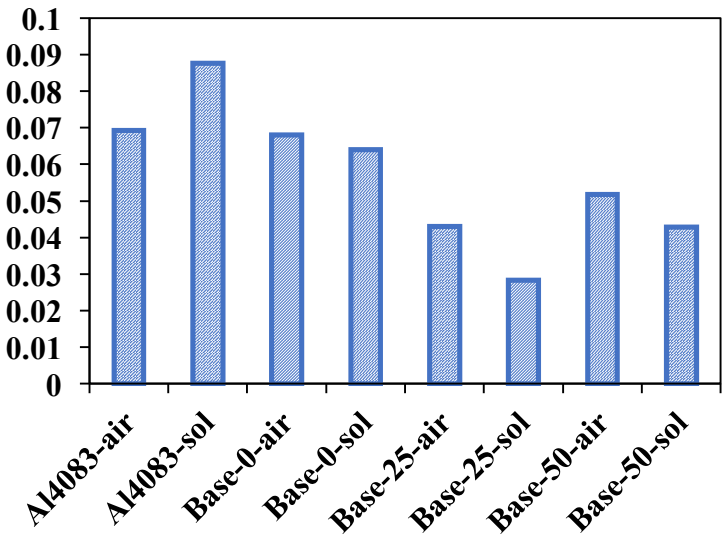

Figure 3-11. The peak intensity ratio of PbI:$MAPbI_3$(110) of $MAPbI_3$ films fabricated on commercial Al 4083 PEDOT:PSS and synthesized Base-0, Base-25 and Base-50 PEDOT-MeCl:PSS films annealed in air and in solvent toluene vapor.

Perovskite crystallization becomes better on the PEDOT-MeCl:PSS prepared under toluene vapor annealing. With less PbI_2, larger grain size, fewer grain boundaries and fewer defects on the active layer, the solar cell is going to have a better device performance on the solvent-annealed PEDOT-MeCl:PSS layer.

3.4 PHOTOVOLTAIC PERFORMANCE OF $MAPbI_3$ PEROVSKITE SOLAR CELLS WITH PEDOT-MeCl:PSS HTLS

The planar PVSCs in this study were structured as glass/ITO/PEDOT-MeCl:PSS/$MAPbI_3$/ $PC_{60}BM$/ BCP/Ag, as shown in **Figure 3-12e**. **Figure 3-12 a, b, c, d** shows the summary of Voc, Jsc, FF and PCE of the optimized $MAPbI_3$ devices using different HTLs. There is no obvious increase of Voc for solvent annealed HTLs because of the high film quality. The decrease of Voc for Base-25 after solvent annealing is ascribed as the result of the little degradation shown in SEM images. However, there's a noticeable increase of Jsc for not only PEDOT:PSS and PEDOT-MeCl:PSS. For AI4083, the Jsc increased from11.37 mA/cm^2 to 13.74 mA/cm^2 after solvent annealing. For Base-0, the Jsc increased from 9.64 mA/cm^2 to 12.92 mA/cm^2. for Base-25, the Jsc increased from 12.98 mA/cm^2 to 14.48 mA/cm^2, and for Base-50 the Jsc increased from 12.74 mA/cm^2 to 13.24 mA/cm^2. Besides, the FF has been enhanced after solvent annealing. The FF of AI4083 annealed in toluene environment reached to a remarkable value of 0.83. Base-0 sample's FF increased from 0.73 to 0.75, and for Base-25, it grew from 0.59 to 0.63, and for Base-0 it grew from 0.71 to 0.72. The increase of both Jsc and FF lead to an obvious enhancement of device PCE. First, the Jsc enhancement is in good agreement with the quinoid to benzoid ratio in Raman spectra. The Jsc is higher for devices fabricated on HTLs with larger Q/B values. This is because of the stronger hole mobility induced by the phase separation that caused by the solvent annealing method. The larger grain size of $MAPbI_3$ will lead to the increase of Jsc and FF because of less

grain boundaries and defects. The less degradation of $MAPbI_3$ on solvent annealed HTLs also gives the device a better performance.

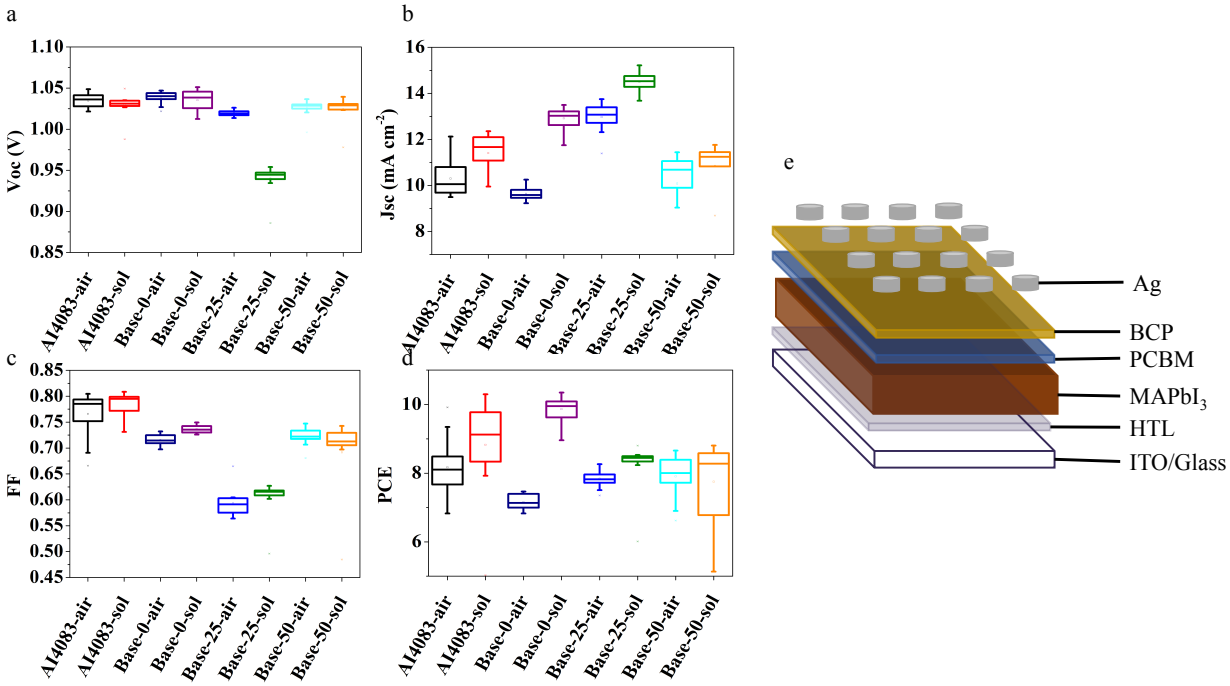

Figure 3-12. Summary of device performance of devices fabricated on different HTLs and device structures. a, Voc summary of devices fabricated on AI4083, Base-0, Base-25, Base-50 annealed in air and toluene vapor environment. b, Jsc summary of devices fabricated on AI4083, Base-0, Base-25, Base-50 annealed in air and toluene vapor environment. c, FF summary of devices fabricated on AI4083, Base-0, Base-25, Base-50 annealed in air and toluene vapor environment. d, PCE summary of devices fabricated on AI4083, Base-0, Base-25, Base-50 annealed in air and toluene vapor environment. e, device structure.

The photocurrent hysteresis was observed by changing the scanning directions, as shown in **Fig 13**. For Base-25 and Base-50, the hysteresis is negligible before and after solvent annealing. While for AI4083, the hysteresis is noticeable when HTL was annealed in air, but it became

negligible after solvent annealing. The absence of obvious photocurrent hysteresis is commonly believed as the result of the larger grain size and less defects on $MAPbI_3$ thin films, and charges traps at the film surface and grain boundaries are well passivated[7].

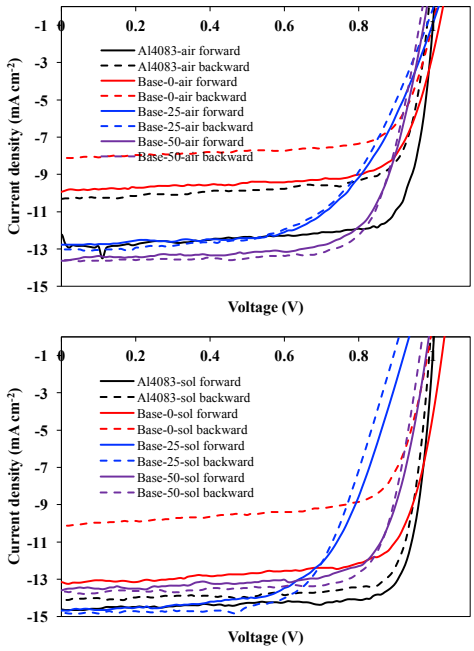

Figure 3-13. Device hysteresis of $MAPbI_3$ perovskite solar cells on different HTLs

To gain more insight into the contributions of different HTLs, we investigated the charge extraction and the dominant recombination mechanisms that influences photovoltaic performance of PVSCs. First, we measured the time-resolved photoluminescence (TRPL) decays of MAPbI3 thin films fabricated on glass (pristine), Base-25 and Base-50 PEDOT-MeCl:PSS, and commercial Al 4083 PEDOT:PSS films annealed in air and in solvent toluene vapor (**Figure 3-14**). The PL decay should be representative of recombination or depopulation of electrons and holes from the perovskite film. The increase in lifetime indicates reduction in nonradiative recombination in the perovskite film, whereas the shortened lifetime suggests introduction of nonradiative recombination centers within the perovskite film[5, 11].

The PL decay curves were fitted using a biexponential equation (**eq 1**).

$$I(t) = A_1 \exp(\frac{t}{\tau_1}) + A_2 \exp(\frac{t}{\tau_2}) \quad (1)$$

The average decay time (τ_{avg}) are estimated with the τ_i and A_i values from the fitted curve date (**Figure 3-15**) using **eq 2**.

$$\tau_{avg} = \frac{\Sigma A_i \tau_i^2}{\Sigma A_i \tau_i} \quad (2)$$

Perovskite fabricated on glass only (pristine) exhibits an average decay time (τ_m) of 28.73 ns. while it increased to 6.03 ns when it was disposed on top of PEDOT:PSS annealed in air. However, it decreased to 5.37 ns when it was disposed on top of PEDOT:PSS annealed in toluene vapor environment because of the degradation of $MAPbI_3$. The lifetimes for PEDOT-MeCl:PSS samples are shorter than PEDOT:PSS, but it increased after solvent annealing. For Base-25, it increased from 2.83 to 3.68 ns, and for Base-50, it increased from 1.95 to 2.60 ns. Time resolved photoluminescence decay with different HTLs showed a bi-exponential decay with a fast and a slow component. Previous studies of charge recombination in perovskite films suggests that the fast decay process is caused by bimolecular recombination of photo-generated free carriers, and the slow decay process is attributed mainly to trap-assisted recombination[48, 49]. Here the solvent-annealing method of HTLs mainly impact the slow decay process, which means the solvent annealed HTLs helps to decrease the charge traps at the interface, which contributes to the high Jsc value for the PVSCs using solvent-annealed HTLs.

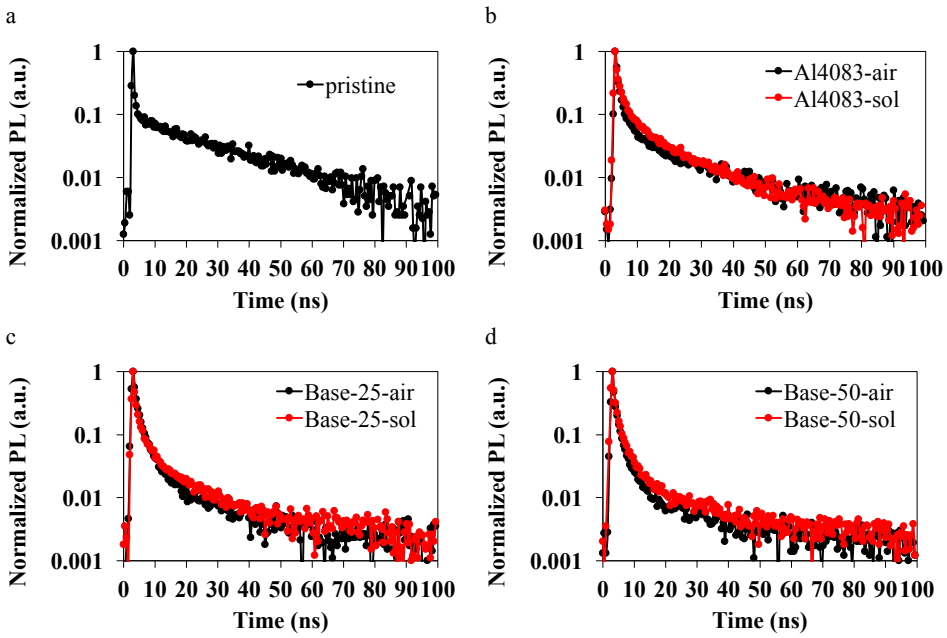

Figure 3-14. Time-resolved photoluminescence (TRPL) decay spectra of $MAPbI_3$ perovskite films fabricated on glass (pristine) (a), and commercial Al 4083 PEDOT:PSS annealed in air and toluene vapor (b) and synthesized Base-25 (c) and Base-50 (d) PEDOT-MeCl:PSS HTLs annealed in air and solvent toluene vapor, respectively.

Table 3-4. Fitting Decay Times of $MAPbI_3$ Perovskite Films with Different HTLs

HTLs	τ_1 (ns)	τ_2 (ns)	τ_m (ns)
Al4083-air	0.81	9.89	6.03
Al4083-sol	0.65	6.92	5.37
Base-25-air	0.68	3.84	2.83
Base-25-sol	0.55	5.14	3.68
Base-50-air	0.47	2.63	1.95
Base-50-sol	0.58	3.65	2.60
Pristine	4.65	30.17	28.73

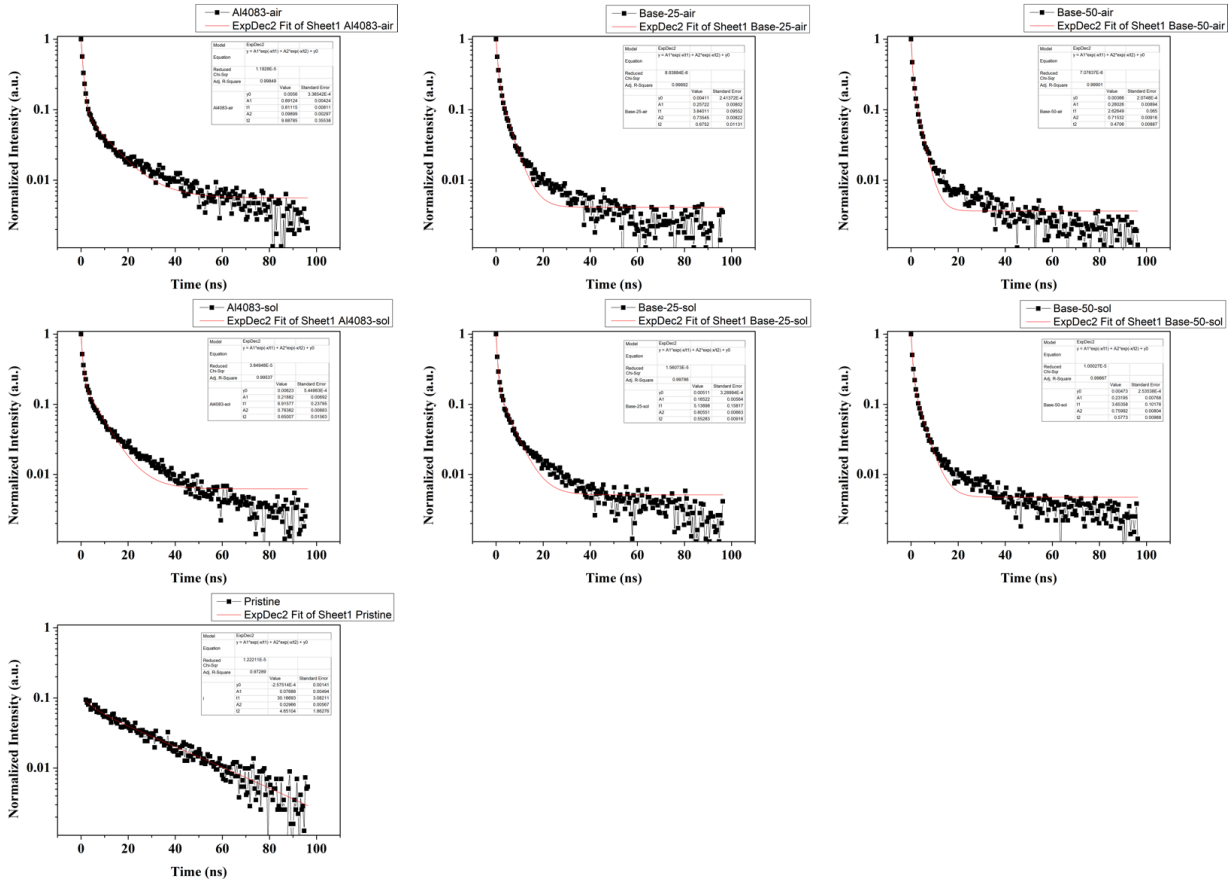

Figure 3-15. TRPL fitting results for $MAPbI_3$ films fabricated on glass (pristine), commercial Al 4083 PEDOT:PSS and synthesized Base-0, Base-25 and Base-50 PEDOT-MeCl:PSS films annealed in air and in solvent toluene vapor.

The increased Jsc of the solvent-annealed HTLs-based devices should be attributed to lower recombination kinetics. To verify this hypothesis, we have further studied the light intensity dependence of the J-V characteristics of the PVSCs to probe the dominant recombination mechanism. **Figure 3-16** presents the power law dependence of the Jsc with light intensity (e). Jsc is liner with illuminated light intensity, indicating there is no substantial space charge buildup increasing the light intensity. Furthermore, a linear fit of the Jsc plot yields a scaling exponent α<1, this means the charge carrier losses are dominated by bimolecular recombination of electrons

and holes[50]. For Base-0 and Base-25, α increased after solvent annealing, the higher slope value indicates that the solvent annealing method mitigates the interfacial recombination loss that the HTL/$MAPbI_3$ interface[7, 50, 51] .

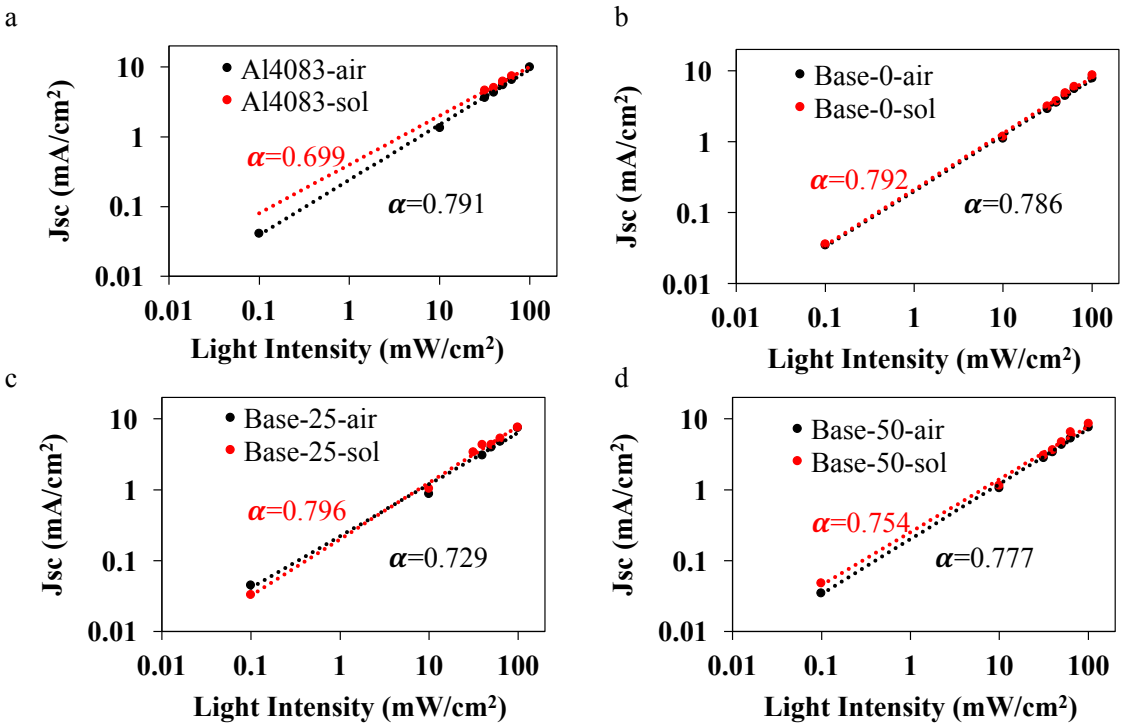

Figure 3-16. Measured Jsc of PVSCs with different HTLs plotted as a function of light intensity in a double logarithmic scale (dots). Fitting of Jsc and light intensity (I) to the power law Jsc $\propto I^{\alpha}$ (dashed lines) yields the values of α.

Since all of the photo-generated charge carriers in the perovskite layer will recombine within the cell under open-circuit conditions, studying the relation between the Voc and the light intensity is a powerful tool to probe the recombination mechanisms precisely[51]. Voc increases linearly with the increase of the logarithmic light intensity. When the Voc equals the applied voltage, the internal electrical field within the device is equal to zero. The field dependence of the photocurrent is of no importance. A simple Shockley model was used to fit the liner relationship

between Voc and logarithmic power (**eq.3**)[52]. The ideal factor (n) was determined for each sample using different HTLs.

$$Voc \propto \frac{nk_BT}{q} \ln\left[\frac{Jph(Voc)}{J_0}\right] \quad (3)$$

Where J_{ph} is the photocurrent.

Generally, if bimolecular recombination is dominant, the slope of Voc versus light intensity will be close to k_BT/q, where k_B is the Bolzmann constant, T is the kelvin temperature, and q is the electron charge. While the slope is greater than k_BT/q, Voc will become strongly depend on light intensity, additional interfacial trap-assisted Shockley-Read-Hall (SRH) recombination is involved[53]. As shown in **Figure 3-17**, the ideality factor was determined to be 1.538 for $MAPbI_3$ films on air annealed Al4083 PEDOT:PSS, but the value decreased to 1.351 when perovskite was formed on the toluene vapor annealed PEDOT:PSS. For PEDOT-MeCl:PSS HTLs, including Base-0, Base-25, and Base-50, the slope of their fitting curves are closer to k_BT/q after solvent annealing. For $MAPbI_3$ on solvent annealed Base-0 and Base-25, their ideal factors are 1.145 and 1.004, respectively. As a consequence, we can conclude that solvent-annealed PEDOT-MeCl:PSS HTLs effectively reduces the monomolecular SRH recombination. For $MAPbI_3$ deposit on Base-50 HTLs, the ideal factors are smaller than 1 for air-annealed and solvent annealed samples, this is because the data points are not evenly distributed, resulting in inaccurate fitting. But it can be seen from the figure that the slope is closer to 1 for solvent-annealed sample, which proves that the surface after solvent annealing can reduce the monomolecular recombination.

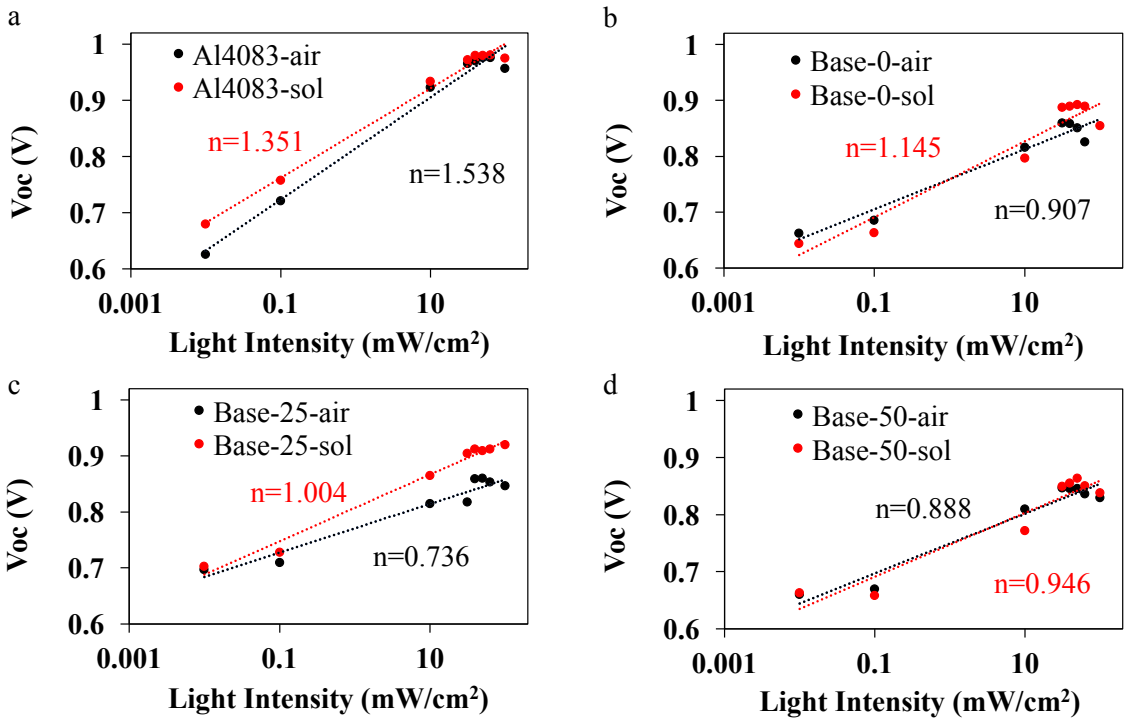

Figure 3-17. Voc as a function of logarithmic scaled light intensity. A fit of Voc and logarithmic light intensity to the simple Shockley equation is shown.

Chapter 4. CONCLUSION

In summary, we demonstrated that the PEDOT-MeCl:PSS is an ideal HTL for perovskite solar cells. The presence of chlorine functional groups in the HTL makes large grain sizes of $MAPbI_3$ and less PbI_2, particularly, on the PEDOT-MeCl:PSS annealed in toluene vapor environment. We also found that the solvent annealing of PEDOT-MeCl:PSS thin films plays a very important role in improving the PCE of perovskite solar cells. Perovskite solar cells made with the solvent annealed PEDOT-MeCl:PSS HTLs exhibited better PCEs because of the enlarged Jsc and FF. To guide the design of new hole transport materials, further improvement of the interfacial defects between HTL and perovskite is desired by understanding the defects between PEDOT-MeCl and $MAPbI_3$, including the type, concentration and distribution of interfacial defects. The introduction of chloride functional group on PEDOT backbone could offer a mean to improve the efficiency of perovskite solar cells and to stabilize perovskite materials and solar cells.

REFERENCE

1. Zhang, H.; Azimi, H.; Hou, Y.; Ameri, T.; Przybilla, T.; Spiecker, E.; Kraft, M.; Scherf, U.; Brabec, C. J., Improved High-Efficiency Perovskite Planar Heterojunction Solar Cells via Incorporation of a Polyelectrolyte Interlayer. *Chemistry of Materials* **2014,** *26* (18), 5190-5193.
2. Wehrenfennig, C.; Eperon, G. E.; Johnston, M. B.; Snaith, H. J.; Herz, L. M., High Charge Carrier Mobilities and Lifetimes in Organolead Trihalide Perovskites. *Advanced Materials* **2014,** *26* (10), 1584-1589.
3. Yip, H. L.; Jen, A. K. Y., Recent advances in solution-processed interfacial materials for efficient and stable polymer solar cells. *Energy & Environmental Science* **2012,** *5* (3), 5994-6011.
4. Malinkiewicz, O.; Yella, A.; Lee, Y. H.; Espallargas, G. M.; Graetzel, M.; Nazeeruddin, M. K.; Bolink, H. J., Perovskite solar cells employing organic charge-transport layers. *Nature Photonics* **2014,** *8* (2), 128-132.
5. Zuo, L. J.; Guo, H. X.; deQuilettes, D. W.; Jariwala, S.; De Marco, N.; Dong, S. Q.; DeBlock, R.; Ginger, D. S.; Dunn, B.; Wang, M. K.; Yang, Y., Polymer-modified halide perovskite films for efficient and stable planar heterojunction solar cells. *Science Advances* **2017,** *3* (8).
6. Jiang, Q.; Zhao, Y.; Zhang, X.; Yang, X.; Chen, Y.; Chu, Z.; Ye, Q.; Li, X.; Yin, Z.; You, J., - Surface passivation of perovskite film for efficient solar cells. **2019**.
7. Chen, H. L.; Fu, W. F.; Huang, C. Y.; Zhang, Z. Q.; Li, S. X.; Ding, F. Z.; Shi, M. M.; Li, C. Z.; Jen, A. K. Y.; Chen, H. Z., Molecular Engineered Hole-Extraction Materials to Enable Dopant-Free, Efficient p-i-n Perovskite Solar Cells. *Advanced Energy Materials* **2017,** *7* (18).
8. Ball, J. M.; Lee, M. M.; Hey, A.; Snaith, H. J., Low-temperature processed meso-superstructured to thin-film perovskite solar cells. *Energy & Environmental Science* **2013,** *6* (6), 1739-1743.
9. Jeon, N. J.; Noh, J. H.; Kim, Y. C.; Yang, W. S.; Ryu, S.; Seok, S. I., Solvent engineering for high-performance inorganic-organic hybrid perovskite solar cells. *Nature Materials* **2014,** *13* (9), 897-903.
10. Xue, Q. F.; Hu, Z. C.; Liu, J.; Lin, J. H.; Sun, C.; Chen, Z. M.; Duan, C. H.; Wang, J.; Liao, C.; Lau, W. M.; Huang, F.; Yip, H. L.; Cao, Y., Highly efficient fullerene/perovskite planar heterojunction solar cells via cathode modification with an amino-functionalized polymer interlayer (vol 2, pg 19598, 2014). *Journal of Materials Chemistry A* **2017,** *5* (13), 6328-6328.
11. Stranks, S. D.; Eperon, G. E.; Grancini, G.; Menelaou, C.; Alcocer, M. J. P.; Leijtens, T.; Herz, L. M.; Petrozza, A.; Snaith, H. J., Electron-Hole Diffusion Lengths Exceeding 1 Micrometer in an Organometal Trihalide Perovskite Absorber. *Science* **2013,** *342* (6156), 341-344.
12. Xing, G. C.; Mathews, N.; Sun, S. Y.; Lim, S. S.; Lam, Y. M.; Gratzel, M.; Mhaisalkar, S.; Sum, T. C., Long-Range Balanced Electron- and Hole-Transport Lengths in Organic-Inorganic CH3NH3PbI3. *Science* **2013,** *342* (6156), 344-347.
13. Jeng, J. Y.; Chiang, Y. F.; Lee, M. H.; Peng, S. R.; Guo, T. F.; Chen, P.; Wen, T. C., CH3NH3PbI3 Perovskite/Fullerene Planar-Heterojunction Hybrid Solar Cells. *Advanced Materials* **2013,** *25* (27), 3727-3732.
14. Liang, P. W.; Liao, C. Y.; Chueh, C. C.; Zuo, F.; Williams, S. T.; Xin, X. K.; Lin, J. J.; Jen, A. K. Y., Additive Enhanced Crystallization of Solution-Processed Perovskite for Highly Efficient Planar-Heterojunction Solar Cells. *Advanced Materials* **2014,** *26* (22), 3748-3754.

15. Chueh, C. C.; Li, C. Z.; Jen, A. K. Y., Recent progress and perspective in solution-processed Interfacial materials for efficient and stable polymer and organometal perovskite solar cells. *Energy & Environmental Science* **2015,** *8* (4), 1160-1189.
16. Xue, Q. F.; Sun, C.; Hu, Z. C.; Huang, F.; Yip, H. L.; Cao, Y., Recent Advances in Perovskite Solar Cells: Morphology Control and Interfacial Engineering. *Acta Chimica Sinica* **2015,** *73* (3), 179-192.
17. Shao, Y. H.; Xiao, Z. G.; Bi, C.; Yuan, Y. B.; Huang, J. S., Origin and elimination of photocurrent hysteresis by fullerene passivation in CH3NH3PbI3 planar heterojunction solar cells. *Nature Communications* **2014,** *5*.
18. Bai, Y.; Meng, X. Y.; Yang, S. H., Interface Engineering for Highly Efficient and Stable Planar p-i-n Perovskite Solar Cells. *Advanced Energy Materials* **2018,** *8* (5).
19. Sun, K.; Zhang, S. P.; Li, P. C.; Xia, Y. J.; Zhang, X.; Du, D. H.; Isikgor, F. H.; Ouyang, J. Y., Review on application of PEDOTs and PEDOT: PSS in energy conversion and storage devices. *Journal of Materials Science-Materials in Electronics* **2015,** *26* (7), 4438-4462.
20. Zhang, F. L.; Johansson, M.; Andersson, M. R.; Hummelen, J. C.; Inganas, O., Polymer photovoltaic cells with conducting polymer anodes. *Advanced Materials* **2002,** *14* (9), 662-665.
21. Yue, G. T.; Wu, J. H.; Xiao, Y. M.; Lin, J. M.; Huang, M. L.; Lan, Z.; Fan, L. Q., Functionalized graphene/poly(3,4-ethylenedioxythiophene): polystyrenesulfonate as counter electrode catalyst for dye-sensitized solar cells. *Energy* **2013,** *54*, 315-321.
22. Villers, D.; Jobin, D.; Soucy, C.; Cossement, D.; Chahine, R.; Breau, L.; Belanger, D., The influence of the range of electroactivity and capacitance of conducting polymers on the performance of carbon conducting polymer hybrid supercapacitor. *Journal of the Electrochemical Society* **2003,** *150* (6), A747-A752.
23. Guo, Z. Y.; Qiao, Y. C.; Liu, H.; Ding, C. M.; Zhu, Y.; Wan, M. X.; Jiang, L., Self-assembled hierarchical micro/nano-structured PEDOT as an efficient oxygen reduction catalyst over a wide pH range. *Journal of Materials Chemistry* **2012,** *22* (33), 17153-17158.
24. Luo, J. J.; Billep, D.; Waechtler, T.; Otto, T.; Toader, M.; Gordan, O.; Sheremet, E.; Martin, J.; Hietschold, M.; Zahnd, D. R. T.; Gessner, T., Enhancement of the thermoelectric properties of PEDOT:PSS thin films by post-treatment. *Journal of Materials Chemistry A* **2013,** *1* (26), 7576-7583.
25. Sekitani, T.; Nakajima, H.; Maeda, H.; Fukushima, T.; Aida, T.; Hata, K.; Someya, T., Stretchable active-matrix organic light-emitting diode display using printable elastic conductors. *Nature Materials* **2009,** *8* (6), 494-499.
26. Benight, S. J.; Wang, C.; Tok, J. B. H.; Bao, Z. A., Stretchable and self-healing polymers and devices for electronic skin. *Progress in Polymer Science* **2013,** *38* (12), 1961-1977.
27. Chen, Q.; Zhou, H. P.; Fang, Y. H.; Stieg, A. Z.; Song, T. B.; Wang, H. H.; Xu, X. B.; Liu, Y. S.; Lu, S. R.; You, J. B.; Sun, P. Y.; McKay, J.; Goorsky, M. S.; Yang, Y., The optoelectronic role of chlorine in CH3NH3PbI3(Cl)-based perovskite solar cells. *Nature Communications* **2015,** *6*.
28. deQuilettes, D. W.; Vorpahl, S. M.; Stranks, S. D.; Nagaoka, H.; Eperon, G. E.; Ziffer, M. E.; Snaith, H. J.; Ginger, D. S., Impact of microstructure on local carrier lifetime in perovskite solar cells. *Science* **2015,** *348* (6235), 683-686.
29. Scavetta, E.; Mazzoni, R.; Mariani, F.; Margutta, R. G.; Bonfiglio, A.; Demelas, M.; Fiorilli, S.; Marzocchi, M.; Fraboni, B., Dopamine amperometric detection at a ferrocene clicked PEDOT: PSS coated electrode. *Journal of Materials Chemistry B* **2014,** *2* (19), 2861-2867.

30. Elschner, A., *PEDOT : principles and applications of an intrinsically conductive polymer*. Boca Raton, FL : CRC Press: Boca Raton, FL, 2011.
31. Wang, Q.; Chueh, C. C.; Eslamian, M.; Jen, A. K. Y., Modulation of PEDOT:PSS pH for Efficient Inverted Perovskite Solar Cells with Reduced Potential Loss and Enhanced Stability. *Acs Applied Materials & Interfaces* **2016,** *8* (46), 32068-32076.
32. Ouyang, B. Y.; Chi, C. W.; Chen, F. C.; Xi, Q. F.; Yang, Y., High-conductivity poly (3,4-ethylenedioxythiophene): poly(styrene sulfonate) film and its application in polymer optoelectronic devices. *Advanced Functional Materials* **2005,** *15* (2), 203-208.
33. Crispin, X.; Jakobsson, F. L. E.; Crispin, A.; Grim, P. C. M.; Andersson, P.; Volodin, A.; van Haesendonck, C.; Van der Auweraer, M.; Salaneck, W. R.; Berggren, M., The origin of the high conductivity of poly(3,4-ethylenedioxythiophene)-poly(styrenesulfonate) (PEDOT- PSS) plastic electrodes. *Chemistry of Materials* **2006,** *18* (18), 4354-4360.
34. Ghosh, S.; Inganas, O., Nano-structured conducting polymer network based on PEDOT-PSS. *Synthetic Metals* **2001,** *121* (1-3), 1321-1322.
35. Bi, C.; Wang, Q.; Shao, Y. C.; Yuan, Y. B.; Xiao, Z. G.; Huang, J. S., Non-wetting surface-driven high-aspect-ratio crystalline grain growth for efficient hybrid perovskite solar cells. *Nature Communications* **2015,** *6*.
36. Zhao, D. W.; Sexton, M.; Park, H. Y.; Liu, S. Y.; Baure, G.; Nino, J. C.; So, F., High-Efficiency Solution-Processed Planar Perovskite Solar Cells with a Polymer Hole Transport Layer (vol 5, 1401855, 2015). *Advanced Energy Materials* **2015,** *5* (6).
37. Kim, J. Y.; Jung, J. H.; Lee, D. E.; Joo, J., Enhancement of electrical conductivity of poly(3,4-ethylenedioxythiophene)/poly(4-styrenesulfonate) by a change of solvents. *Synthetic Metals* **2002,** *126* (2-3), 311-316.
38. Singh, V.; Arora, S.; Arora, M.; Sharma, V.; Tandon, R. P., Characterization of doped PEDOT: PSS and its influence on the performance and degradation of organic solar cells. *Semiconductor Science and Technology* **2014,** *29* (4).
39. Xiong, S. X.; Fu, J. L.; Li, Z. F.; Shi, Y. J.; Wang, X. Q.; Chu, J.; Gong, M.; Wu, B. H., Modulating the Electrochromic Performances of Transmissive and Reflective Devices Using N, N-Dimethyl Formamide Modified Poly(3,4-Ethylenedioxythiophene)/Poly(Styrene Sulfonate) Blend as Active Layers. *Journal of Macromolecular Science Part B-Physics* **2015,** *54* (7), 799-810.
40. Chiu, W. W.; Travas-Sejdic, J.; Cooney, R. P.; Bowmaker, G. A., Spectroscopic and conductivity studies of doping in chemically synthesized poly(3,4-ethylenedioxythiophene). *Synthetic Metals* **2005,** *155* (1), 80-88.
41. Park, H. S.; Ko, S. J.; Park, J. S.; Kim, J. Y.; Song, H. K., Redox-active charge carriers of conducting polymers as a tuner of conductivity and its potential window. *Scientific Reports* **2013,** *3*.
42. Kang, T. G.; Park, J. K.; Yun, G. H.; Choi, H. H.; Lee, H. J.; Yook, J. G., A real-time humidity sensor based on a microwave oscillator with conducting polymer PEDOT:PSS film. *Sensors and Actuators B-Chemical* **2019,** *282*, 145-151.
43. Xia, Y. J.; Ouyang, J. Y., PEDOT:PSS films with significantly enhanced conductivities induced by preferential solvation with cosolvents and their application in polymer photovoltaic cells. *Journal of Materials Chemistry* **2011,** *21* (13), 4927-4936.
44. Ouyang, J.; Xu, Q. F.; Chu, C. W.; Yang, Y.; Li, G.; Shinar, J., On the mechanism of conductivity enhancement in poly (3,4-ethylenedioxythiophene): poly(styrene sulfonate) film through solvent treatment. *Polymer* **2004,** *45* (25), 8443-8450.

45. Farah, A. A.; Rutledge, S. A.; Schaarschmidt, A.; Lai, R.; Freedman, J. P.; Helmy, A. S., Conductivity enhancement of poly(3,4-ethylenedioxythiophene)-poly(styrenesulfonate) films post-spincasting. *Journal of Applied Physics* **2012,** *112* (11).
46. Tosado, G. A.; Lin, Y. Y.; Zheng, E. J.; Yu, Q. M., Impact of cesium on the phase and device stability of triple cation Pb-Sn double halide perovskite films and solar cells. *Journal of Materials Chemistry A* **2018,** *6* (36), 17426-17436.
47. Wang, W.; Zhang, Z. B.; Cai, Y. Y.; Chen, J. S.; Wang, J. M.; Huang, R. Y.; Lu, X. B.; Gao, X. S.; Shui, L. L.; Wu, S. J.; Liu, J. M., Enhanced performance of CH3NH3PbI3-xClx perovskite solar cells by CH3NH3I modification of TiO2-perovskite layer interface. *Nanoscale Research Letters* **2016,** *11*.
48. Son, D.-Y.; Lee, J.-W.; Choi, Y. J.; Jang, I.-H.; Lee, S.; Yoo, P. J.; Shin, H.; Ahn, N.; Choi, M.; Kim, D.; Park, N.-G., - Self-formed grain boundary healing layer for highly efficient CH3 NH3 PbI3 perovskite solar cells. **2016,** - *1*, -.
49. Chen, Q.; Zhou, H. P.; Song, T. B.; Luo, S.; Hong, Z. R.; Duan, H. S.; Dou, L. T.; Liu, Y. S.; Yang, Y., Controllable Self-Induced Passivation of Hybrid Lead Iodide Perovskites toward High Performance Solar Cells. *Nano Letters* **2014,** *14* (7), 4158-4163.
50. Riedel, I.; Parisi, J.; Dyakonov, V.; Lutsen, L.; Vanderzande, D.; Hummelen, J. C., Effect of temperature and illumination on the electrical characteristics of polymer-fullerene bulk-heterojunction solar cells. *Advanced Functional Materials* **2004,** *14* (1), 38-44.
51. Zhang, H.; Cheng, J. Q.; Lin, F.; He, H. X.; Mao, J.; Wong, K. S.; Jen, A. K. Y.; Choy, W. C. H., Pinhole-Free and Surface-Nanostructured NiOx Film by Room-Temperature Solution Process for High-Performance Flexible Perovskite Solar Cells with Good Stability and Reproducibility. *Acs Nano* **2016,** *10* (1), 1503-1511.
52. Zhu, L. Z.; Richardson, B. J.; Yu, Q. M., Inverted hybrid CdSe-polymer solar cells adopting PEDOT:PSS/MoO3 as dual hole transport layers. *Physical Chemistry Chemical Physics* **2016,** *18* (5), 3463-3471.
53. Jung, J. W.; Chueh, C. C.; Jen, A. K. Y., High-Performance Semitransparent Perovskite Solar Cells with 10% Power Conversion Efficiency and 25% Average Visible Transmittance Based on Transparent CuSCN as the Hole-Transporting Material. *Advanced Energy Materials* **2015,** *5* (17).